Simulations of planets in post–Common Envelope Binary Systems with the FLASH code

vorgelegt von
Christiane Schneide

Hamburg, 2017

Family

Simulations of planets in post–Common Envelope Binary Systems with the FLASH code

Abstract

I study systems with planets in post–common envelope binaries (PCEBs) to analyze the question of planet formation and planetary dynamics in this kind of systems with three-dimensional hydrodynamical simulations.

I choose NN Serpentis as an exemplary system. It consists of a white dwarf (WD) primary component of $0.535 \pm 0.012\,\mathrm{M_\odot}$ and an M dwarf secondary component of $0.111 \pm 0.004\,\mathrm{M_\odot}$ within a 3hr 7min orbit (Parsons et al., 2010; Haefner et al., 2004). Additionally, the system is supposed to have two planets with masses $(\mathrm{m} \cdot \sin(i))$ and orbital separations of $\sim 7\,\mathrm{M_J}$ and ~ 5.4 AU for planet c and $\sim 1.7\,\mathrm{M_J}$ and ~ 3.4 AU for planet d (Beuermann et al., 2013).

The observation of common envelope (CE) events is difficult because they appear on astrophysically short timescales (~ 1000 years, Ivanova et al. (2013)). Therefore, the current knowledge of structure formation and energy transformation within the envelope is based on numerical simulations. The outcome of these simulations depend on the numerical technique and the initial parameters that are used. Thus, initial parameters for models of the post–CE phase are difficult to determine exactly.

For this reason, I carry out a parameter study. I evaluate simulations depending on the total kinetic energy of the gaseous envelope and the distribution of density and kinetic energy within the envelope.

The simulations show that the survival of first-generation planets which formed before the CE event is possible but strongly depends on interactions with the gaseous envelope. Therefore, planets only remain gravitationally bound in setups with moderate initial kinetic energy.

The scenario of second-generation planet formation is supported by my simulations through the formation of fall-back disks. For similar initial conditions the remaining bound mass within the simulation box is comparable to the analytic result of Schleicher and Dreizler (2014).

The growth of first-generation planets during the CE event is neither confirmed nor ruled out by this study. This effect has to be studied in simulations with higher numerical resolution.

Zusammenfassung

In der Entwicklung von engen Doppelsternen kann es zu einer Phase kommen, in der die Kerne beider Sterne innerhalb einer Gashülle umeinander rotieren. Dies wird die "gemeinsame Hüllenphase" genannt. Da ein Großteil aller Sterne in Doppelsternsystemen oder sogar Mehrfachsternsystemen vorliegt gibt es viele Beispiele für Systeme, die aus der gemeinsamen Hüllenphase hervorgehen. Dazu gehören unter anderem sehr enge Doppelsterne bestehend aus einem Hauptreihenstern und einem Weißen Zwerg. Ein Beispiel für ein solches Systems ist NN Serpentis. Es setzt sich zusammen aus einem Hauptreihenstern mit einer Masse von 0.111 ± 0.004 $M_\odot$ und einem Weißen Zwerg der Masse 0.535 ± 0.012 $M_\odot$. Die Sterne umkreisen das gemeinsame Zentrum mit einer Periode von 3h 7min (Parsons et al., 2010; Haefner et al., 2004). Auf Grund von Schwankungen in der Periodizität der Bedeckung des Weißen Zwerges durch den Hauptreihenstern wurde von Beuermann et al. (2010) die Hypothese aufgestellt, dass zwei Planeten das Doppelsternsystem umkreisen. Diese Hypothese konnte bis heute nicht widerlegt werden. Die aktuellen Werte für Masse und Radius der beiden möglichen Planeten sind ~ 7 M_J und ~ 5.4 AU für Planet c und ~ 1.7 M_J und ~ 3.4 AU für Planet d (Beuermann et al., 2013).

Vorgelegt wird hier eine Parameterstudie, welche die Auswirkung der gemeinsamen Hüllenphase auf die Dynamik eventuell vorhandener Planeten untersucht. Desweiteren wird die Möglichkeit von Planetenentstehung in Überresten der Gashülle studiert. Die Parameterstudie basiert unter anderem auf den Ergebnissen von Ricker and Taam (2008, 2012) und Passy et al. (2012). In den durchgeführten Simulationen variiere ich die gesamte kinetische Energie der Gashülle sowie die Verteilung der kinetischen Energie und der Dichte innerhalb des Gases.

Die durchgeführten Simulationen zeigen, dass sowohl das Überleben der gemeinsamen Hüllenphase für Planeten möglich ist als auch die Entwicklung für Bedingungen zur Planetenentstehung aus Überresten der Hülle.

Planeten der ersten Generation können die Hüllenphase überstehen wenn sie mit dem Gas der Hülle wechselwirken. Damit dieser Effekt stark genug ist darf sich das Gas nicht zu schnell ausbreiten, das bedeutet die kinetische Energie der Hülle darf nicht zu groß sein.

In vielen Simulationen bildet sich aus dem zurückfallenden Gas eine Scheibe um den Doppelstern. Diese bietet gute Bedingungen zur Entstehung von neuen Planeten. Die beobachteten Massen, die am Ende der Simulationen noch an das System gebunden sind, sind verlgeichbar mit dem berechneten Wert in Schleicher and Dreizler (2014) und unterstützen somit die Berechnungen zur Planetenentstehung.

Mit den hier präsentierten Simulationen ist es nicht möglich das Wachstum von Planeten der ersten Generation während der gemeinsamen Hüllenphase zu untersuchen. Somit kann diese Möglichkeit weder bestätigt noch ausgeschlossen werden.

Contents

1
Introduction

PLANETS can be found in various constellations with their host star(s). For example, Doyle et al. (2011) report the detection of a planet orbiting two low-mass stars. Zorotovic and Schreiber (2013) publish a list of planetary candidates orbiting post–common envelope binaries (PCEBs). These are derived from observed variations in the eclipse time of the binary. The history of the systems raises the interest in the existence and formation of planets around PCEBs.

The common envelope (CE) is an important astrophysical process in binary star evolution. It is widely accepted to be the formation channel for many close compact binaries such as high-mass X-ray binaries (Zuo and Li, 2014), progenitors of Type Ia supernovae (Iben and Tutukov, 1984; Kashi and Soker, 2011) and white dwarf/main-sequence (WDMS) binaries (Rebassa-Mansergas et al., 2007). The SDSS WDMS binary catalogue[1] lists more than 3200 systems, more than 200 of which are supposed to have undergone a common envelope phase and be PCEBs.

The theory of CE evolution dates back to the 1970s. The fundamental idea is that the progenitors of PCEB components must once have been larger than the radius of the remnant system. Thus, the two components originally formed at wider separations. During the evolution along the giant

---

[1]White Dwarf-Main Sequence Binaries from the Sloan Digital Sky Survey: www.sdss-wdms.org

branch of the primary, its gaseous envelope engulfed the secondary component and through the transfer of angular momentum and energy with the envelope the angular separation of the binary decreased. This might lead to a merger or the ejection of the envelope, revealing the PCEB.

Recent research includes binary population synthesis studies and numerical simulations of the CE phase in order to determine the energy sources and further physical effects such as drag and disk formation that might influence the outcome of CE evolution.

PCEBs serve as good targets for eclipse timing measurements because they have short orbital periods $\mathcal{O}(\mathrm{days})$ and sharp ingress/ egress features due to the compact nature of the components. Observed period variations can e.g. be attributed to the existence of a third body in the system. In this case the variation should be periodical itself. A discrepancy between later ecplise timing observations and the predicted times from the assumption of a third body often leads to the exclusion of this hypothesis. In this sense, the system NN Serpentis is quite special because seven years after the proposition of the existence of two planets in the WDMS binary system the thesis still holds.

Assuming the planetary hypothesis for NN Serpentis is correct, the question of the origin of these planets is still open. Analytical studies of the planetary orbits under changes of the gravitational potential, describing mass loss during the CE phase, show that first generation planets, formed before the CE phase, would most probably not survive this stage of stellar evolution (Völschow et al., 2014). The formation of second generation planets (after the CE phase) seems to be possible (Schleicher and Dreizler, 2014). As the elapsed time since the end of the CE phase, determined from the cooling time of the WD which has a temperature of 57.000 K, is supposed to be 1.3 Myr the planets in NN Serpentis could be among the youngest planets known with ages $<$ 1 Myr (Beuermann et al., 2010).

Here, I perform numerical simulations of the post–CE phase in order to contribute to the investigation of disk formation with special attention to conditions for planet formation. Furthermore, I analyze the dynamics of first generation planets under the influence of the CE phase.

The structure of this thesis is the following. In chapter 2 I present the underlying principles for the formation of PCEBs. The method used for my simulations is presented in chapter 3. Chapter 4 contains the results of the simulations. Conclusions are drawn in chapter 5.

2

Astrophysical Background

In the following chapter, I give a résumé of the basic theories and concepts which lay the foundations for the performed simulations. These include astrophysical theories on stellar evolution of single and binary stars, in particular the common envelope phase including recent numerical studies by various authors. Furthermore, I summarize the state of research on extrasolar planets.

2.1   Post–Main Sequence stellar evolution of single stars

A star spends most of its lifetime in the main sequence (MS) phase. During this evolutionary phase, central hydrogen burning is the main energy source of the star. The conversion of hydrogen into helium leads to the formation of a small helium core surrounded by a thick hydrogen shell. The ongoing production of helium leads to an increase in mass of the core. When hydrogen is depleted in the central region nuclear burning is restricted to the shell. At this stage, the star leaves the MS. The following detailed stellar evolution highly depends on the mass of the star. For the course of this chapter I will focus on the evolution of a star with $M \approx 2M_\odot$. This represents the evolution for stars with masses between $0.4M_\odot$ and $2.3M_\odot$.

The evolution track of a $2M_\odot$ star is shown in a Hertzsprung-Russell diagram (HRD) in Fig. 2.1.
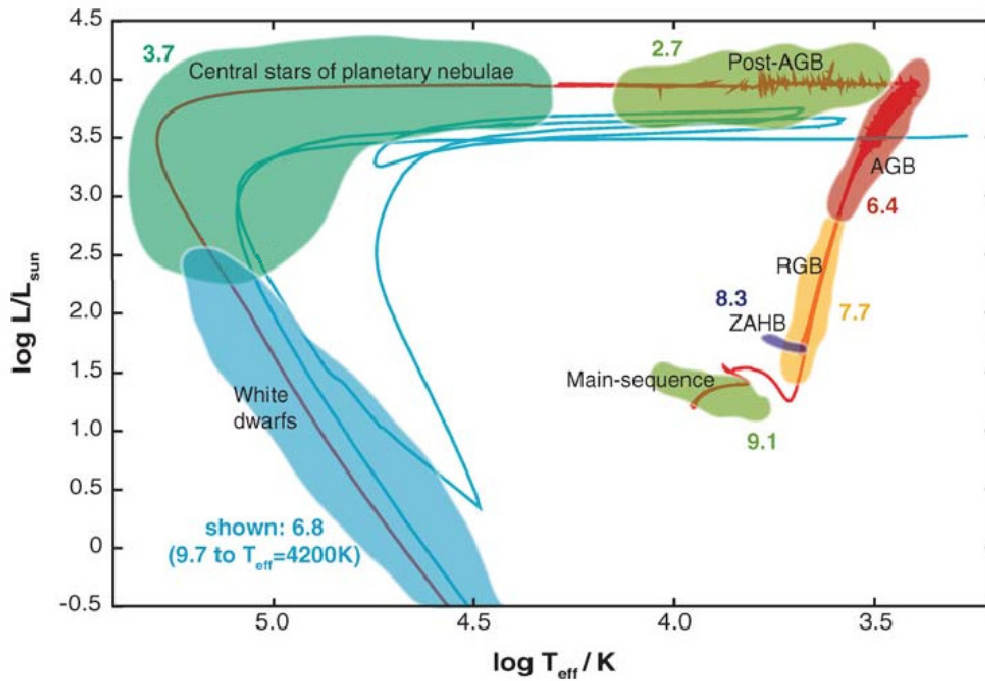
Figure 2.1: Calculated evolution track of a $2\,M_\odot$ star of solar metallicity plotted in an HR diagram. Image taken from Herwig (2005), slightly altered. The authors state, that the oscillatory behavior of the line in the post–AGB phase is caused by numerical convergence difficulties. The blue track represents a born-again evolution shifted to the lower left for better visibility. The numbers displayed at each phase give the log of the time spent in this phase for a $2\,M_\odot$ star in years.

2.1.1   Helium ignition

The helium core of a $2\mathrm{M}_\odot$ star is nearly isothermal at the end of the MS phase, the temperature is determined by the hydrogen-burning shell. Since there is no energy source supporting the core mass against gravity, the star leaves the hydrostatic equilibrium, eq. 2.1. This equates the outwards directed pressure forces with the inwards directed gravitational forces.

$$\frac{dP(r)}{dr} = -\frac{GM_r}{r^2}\rho(r) \tag{2.1}$$

P is the pressure, G the gravitational constant, $\mathrm{M_r}$ is the mass enclosed within the radius r and $\rho(\mathrm{r})$ is the density at this radius. The core contracts slowly. The gravitational energy released in the contraction heats up the envelope which then expands slightly. With increasing core mass due to a supply with helium from the hydrogen burning shell and decreasing core radius the central density rises. For stars with initial mass $> 1.8\mathrm{M}_\odot$ the core is described by an ideal gas, the equation of state (EOS) is given in eq. 2.2. Here, V denotes the volume, N is the number of gas particles in volume V, T is the temperature and $\mathrm{k_B}$ is the Boltzmann constant.

$$PV = Nk_BT \tag{2.2}$$

The contraction of the core directly leads to an increase in temperature until helium burning begins. The critical temperature for helium burning is roughly 10^8 K (Weigert et al., 2010).

For stars with initial mass $\leqslant 1.8\mathrm{M}_\odot$ the electron gas becomes highly degenerate (Herwig, 2005). The EOS for a completely degenerate electron gas in the non-relativistic case is given in equation 2.3 (Kippenhahn and Weigert, 1994). In this equation μ_e denotes the mean molecular weight per free electron.

$$P = 1.0036 \times 10^{13} \times \frac{\rho}{\mu_e}^{5/3} \mathrm{dyn/cm^2} \tag{2.3}$$

The temperature in the core rises with the temperature of the surrounding shell. As the core mass reaches roughly $0.45\mathrm{M}_\odot$ the temperature has risen to 10^8 K and helium is ignited in the core.
Since temperature and pressure are decoupled, the degenerate core cannot expand, therefore the nuclear energy is transformed to internal energy and the temperature in the core rises. This leads

to an increase in energy production in the core. The following peak of the local luminosity, called helium core flash, is almost entirely absorbed by the non-degenerate layers above the core which expand. Due to the high temperature reached in the core the degeneracy is removed and the core expands. Hence, the temperature and energy production rate decrease again.

2.1.2 Red Giant phase

The contraction of the core after core hydrogen burning leads to an increase of the temperature and energy production and thus the hydrogen-burning shell expands. The envelope of the star, scaling with the radius of the hydrogen-burning shell, expands and cools down. Thus, when hydrogen is exhausted in the center, the star advances towards the right side in the HRD. However, there is a lower limit to the effective temperature of a star at ~ 4000 K (Weigert et al., 2010) when the ionisation structure of the star changes. This leads to a decrease in the absorption coefficient and increasing luminosity of the star. The star moves upwards in the HRD. Compared to its time on the main sequence the star has now a very low effective temperature and a huge radius. It is termed a Red Giant (RG).

When helium is ignited the star is temporarily moving backwards in the HRD, creating a slope in the evolution track. This is visible in Fig. 2.1 shortly after the MS phase.

The star leaves the Red Giant Branch when helium is exhausted in the core and moves up in the HRD along the Asymptotic Giant Branch (AGB).

2.1.3 Asymptotic Giant Branch phase

During helium burning carbon and oxygen are created in the core. After helium exhaustion the CO core rapidly contracts and heats up. Helium burning is then restricted to a shell above the core still enclosed by a hydrogen-burning shell and the hydrogen-rich envelope. With the ongoing contraction of the core, the helium-burning shell narrows and the layers above this shell expand and cool down. This leads to a temporary extinction of the hydrogen shell burning. However, the helium burning continues in the underlying shell and expands, thus coming closer to the hydrogen-rich envelope and heating it up. When the temperature again reaches the limit of $\sim 10^8$ K the hydrogen-burning shell reignites. The helium shell shrinks and shell burning becomes unstable, ocurring in thermal pulses, so called helium shell flashes, due to the ongoing

supply with helium from the hydrogen-burning shell. These pulses cause the hydrogen-burning shell to expand and cool down. The outermost layers are only loosely bound to the star and mass loss sets in.

At the end of the Asymptotic Giant Branch phase shell burning is extinguished completely within the shrinking envelope. The remaining envelope mass is expelled and reveals a hot compact central object which will become a white dwarf.

2.1.4   White Dwarf

The compact remnant of a stellar core stops contracting when gravity is counterbalanced by the electron degenerate pressure. At the point of complete degeneracy, the electrons are packed as tightly as possible without violating the Pauli exclusion principle. With increasing density in the core the electron gas becomes more and more relativistic, leading to the EOS as given in equation 2.4 (Kippenhahn and Weigert, 1994). Note that the pressure is now proportional to the density to the power of $\frac{4}{3}$.

$$P = 1.2435 \times 10^{15} \times \frac{\rho}{\mu_e}^{4/3} \text{dyn/cm}^2 \qquad (2.4)$$

Stellar models for WDs composed of non-relativistic degenerate electron gas lead to a mass-radius relation of $R \propto M^{-1/3}$, meaning that the radius shrinks with increasing mass. The limits of this model are $M \to \infty$ and $R \to 0$. Including relativistic effects, the models yield an upper limit for the mass called Chandrasekhar mass M_{Ch}(based on Chandrasekhar (1931)):

$$M_{Ch} = 1.44 M_\odot. \qquad (2.5)$$

Realistic WDs consist of an extremely dense degenerate core and less dense outer layers where the degeneracy is reduced. Energy transport in the central part is dominated by electron conduction leading to an isothermal interior with temperatures around 10^7 K (Kippenhahn and Weigert, 1994). In the outer layers, energy is transported via radiation or convection which is less effective than the electron conduction in the center. Therefore, the temperature drops significantly in the outer layers. The thermal energy of white dwarfs mainly comes from kinetic energy of the nuclei. This can be estimated and combined with its luminosity to calculate the cooling time of WDs, τ_{WD}. Carroll and Ostlie (2006) give a value for $\tau_{\text{WD}} = 170 \times 10^9$ yr with

the remark that this value will be underestimating the cooling time. For recent work on the cooling time of white dwarfs see e.g. Rohrmann et al. (2012).

2.2 Evolution of close binary stars

Stellar binaries and multiple stellar systems are common among different types of populations. Values of the multiplicity fraction range from less than 10% up to almost 80% (e.g. Mason et al., 2009; Janson et al., 2013; Elliott et al., 2014; Ward-Duong et al., 2015). This is shown in Fig. 2.2, plotting the multiplicity fraction over spectral class (Elliott et al., 2014).
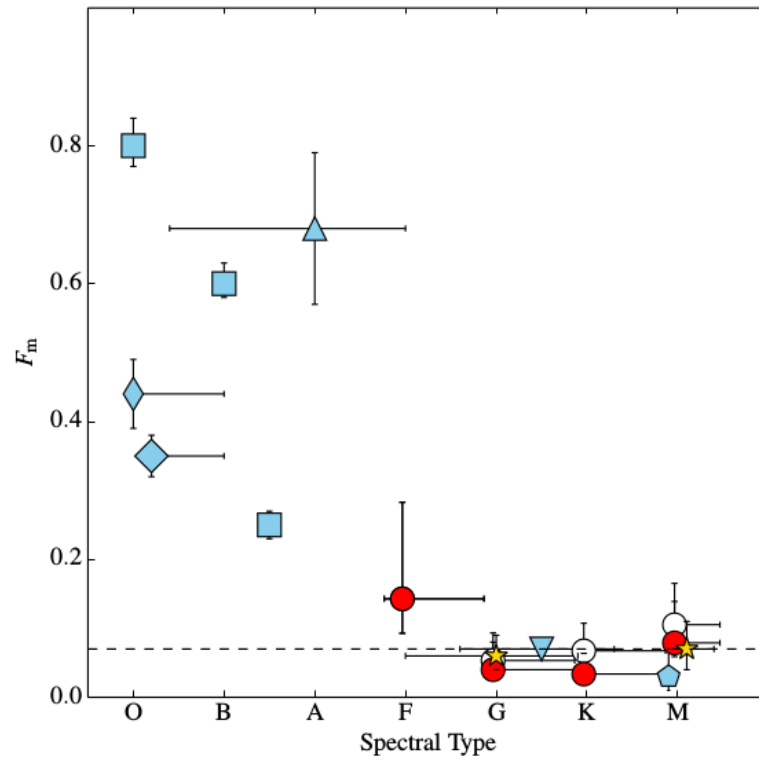

Figure 2.2: Multiplicity fraction of stars in terms of spectral class. Red and white markers are used for Search for Associations Containing Young Stars (SACY) data. Yellow and blue markers represent data from other authors. For more details see Elliott et al. (2014). Spectral class bins are represented with horizontal error bars.

However, most of them are far apart from each other and can be treated as single stars in stellar evolution. The critical separation, according to Carroll and Ostlie (2006), under which both components of the stellar binary have to be taken into account for stellar evolution, is the size of the primary. Here, I focus on the evolution of close binary systems.

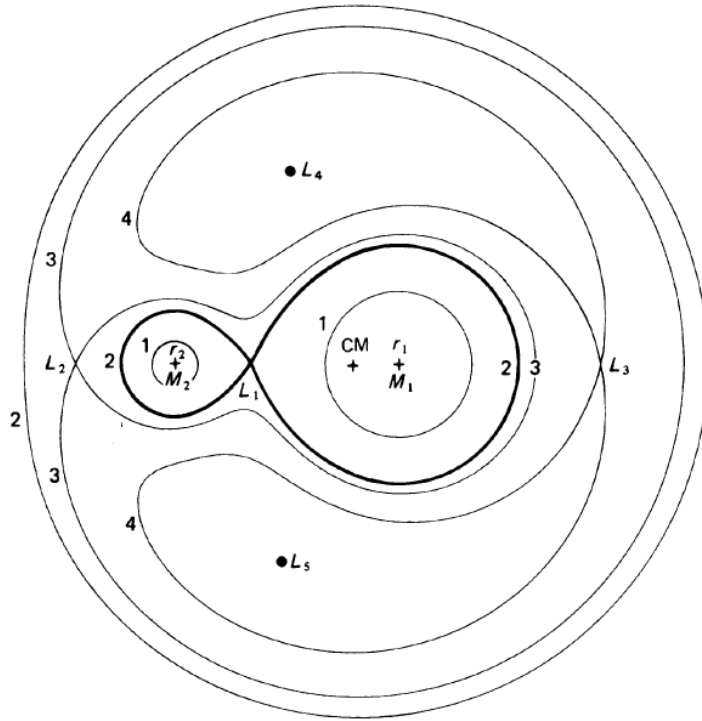More details on binary evolution can be found in Hurley et al. (2002, chapter 2).

Figure 2.3: Equipotential surfaces for a binary system with mass ratio q = 0.25. The + signs represent the positions of the primary M_1 at distance r_1, secondary M_2 at distance r_2 and the center of mass of the system to which the distances are given. The numbers one to four along the lines mark the order of the plotted surfaces starting with the innermost. Also tagged are the Lagrangian points L_1, L_2 and L_3. Image credits: Iben and Livio (1993).

2.2.1   Equipotential surfaces

Compared to single stars, which are spherical, stars in a close binary are disturbed by their companion and have elongated shapes. This is examined in the Roche model, named after the French mathematician Édouard Roche. Due to the close proximity of such a system, the stars will be tidally locked and rotate in circular orbits around their common center of mass. The Roche model considers the total graviational potential of two point masses. Fig 2.3 shows the equipotential surfaces, i.e. surfaces of constant graviational potential Φ, in the orbital plane of the binary for such a constellation.

Due to hydrostatic equilibrium (see eq. 2.1) the pressure and therefore also the density is constant along surfaces of constant Φ. It can be seen that close to the point masses the equipotential surfaces are quasi circular. Moving outwards the surfaces have more and more distorted shapes elongated towards the position of the companion. If a star expands its shape will adjust to the
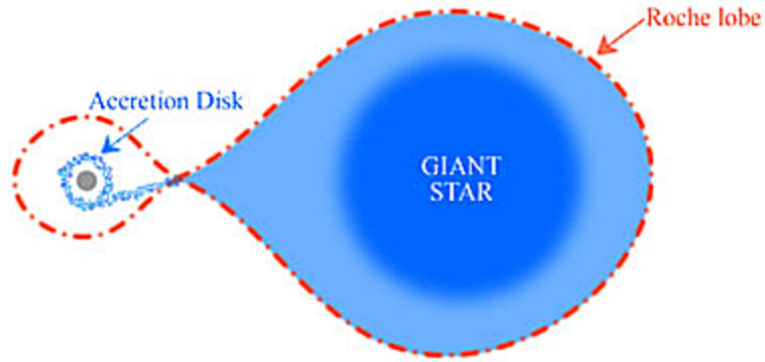
Figure 2.4: Giant star filling its Roche-lobe and transferring mass through L_1 to the secondary where matter accumulates and forms an accretion disk. Image taken from `http://astronomy.swin.edu.au/cosmos/R/roche-lobe+overflow` and rearranged.

equipotential surface to retain equilibrium. The intersection points of equipotential surfaces are called Lagrangian points. The inner Lagrangian point L_1 between the two components determines the limiting volumes called Roche lobes. This can be used to define the effective radius r_L of a star following the notation of Eggleton (1983), see eq. 2.6. Here, the effective radius of a Roche lobe is given in terms of the binary separation. q is the mass ratio of the stars. The derivation of this equation is based on Paczyński (1971).

$$r_L = \frac{0.49q^{2/3}}{0.6q^{2/3} + \ln(1 + q^{1/3})}, 0 < q < \infty \qquad (2.6)$$

2.2.2   Mass transfer and mass loss

After a star fills its Roche lobe it can lose mass through L_1. This mechanism is called Roche-lobe overflow (RLOF). The mass coming through L_1 will rotate in a Keplerian orbit around the companion, potentially forming an accretion disk (Fig. 2.4).

If all the lost mass from the donor is accreted by the accretor then total mass and total orbital angular momentum is conserved. This is the case of conservative mass transfer. The separation of the stars decreases for the case that mass is transferred from the more massive star onto the less massive star ($M_1 > M_2$). If the donor becomes less massive due to mass transfer then the separation can increase again. The equation for the change in orbital period due to conservative mass transfer is given in eq. 2.7 as calculated in Hilditch (2001). M_1 and M_2 are the masses of the

donor and accretor, respectively and P is the orbital period.

$$\frac{\dot{P}}{P} = \frac{3\dot{M_1}(M_1 - M_2)}{M_1 M_2} \tag{2.7}$$

Non-conservative mass transfer includes mass loss and thereby loss of angular momentum. This can be the case when mass transfer after RLOF happens too fast for the accretor on less than a thermal timescale (Iben and Livio, 1993). The material accumulates around the secondary and mass will get lost through the outer Lagrangian point L_2. The orbital period decreases further with the loss of angular momentum, see eq. 2.8 (Hilditch, 2001). M is the sum of M_1 and M_2 and K stands for any mechanisms accounting for angular momentum loss as $K \cdot J$.

$$\frac{\dot{P}}{P} = -\frac{2\dot{M}}{M_1 + M_2} - \frac{3\dot{M_2}(M_1 - M_2)}{M_1 M_2} + 3K \tag{2.8}$$

2.3 Common envelope

The Roche lobes and thereby the radius of the stellar atmospheres adjust to the changes in orbital separation of the binary. Together with non-conservative mass transfer and RLOF of the secondary this can lead to a phase when both stars move within a common envelope (CE).

The idea of CE evolution dates back to Paczynski (1976), citing private communication with Ostriker and Webbink (1975). A detailed review on CE evolution is given in Ivanova et al. (2013). Veras (2016) discuss the effects of CE evolution onto planetary systems, investigating e.g. the accretion of mass by the planetary companion, interactions with asteroids and the impact of stellar radiation.

According to Ivanova et al. (2013) the CE evolution can be split into five phases. This is also supported by Podsiadlowski (2001), e.g. see Fig. 2.5, taken from their paper, which shows the evolution of the radius of the envelope and the position of the secondary over time as result of quasi-hydrostatic simulations. Different phases of the evolution are clearly distinguishable.

2.3.1 The main phases of CE evolution

The five main phases of CE evolution are:

1. Loss of corotation
2. Rapid spiral-in
3. Controlled spiral-in
4. Termination of controlled spiral-in
5. Post–CE evolution

Loss of corotation

Starting with a close stable binary the onset of a CE phase depends amongst others on the evolutionary state as well as the mass ratio of the components. It can be induced, as explained before, by dynamical mass transfer. Further mechanisms are e.g. loss of orbital angular momentum due to gravitational wave radiation (Iben and Livio, 1993). Subsequently, the expanded envelope cannot maintain corotation with the binary.
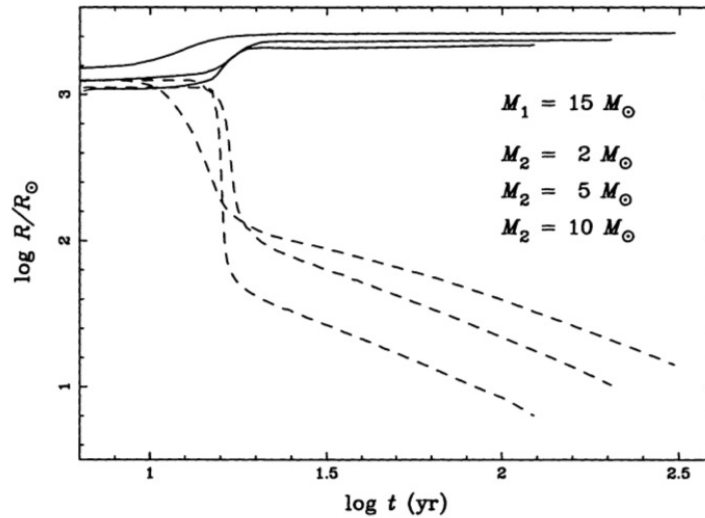
Figure 2.5: Simulations of the spiralling in of secondaries with masses M_2 inside the envelope of a 15 $M_\odot$ primary star by Podsiadlowski (2001). The dashed lines show the estimated position of the secondary inside the envelope. The lines represent simulations with M_2 = 2, 5 and 10 $M_\odot$ from bottom to top at the end of the simulation time. The continuous lines show the radius of the envelope. Distinct phases in the evolution of the binary can be determined.

Rapid spiral-in

Friction between the envelope and the stars leads to the transfer of orbital energy onto the envelope. Thereby, the binary spirals inward and the envelope expands. If sufficient energy is released it may even lead to the ejection of the envelope (e.g. Paczynski, 1976; Podsiadlowski, 2001; Hurley et al., 2002; Ivanova et al., 2013).

Controlled spiral-in

At some point the expansion of the envelope reaches a level the where spiral-in of the binary slows down. This happens when the binding energy of the envelope is comparable to the total orbital energy of the binary (Podsiadlowski, 2001). Further frictional energy which is released by the binary is transported to the surface and radiated away, leading to an increase in luminosity of the envelope (Meyer and Meyer-Hofmeister, 1979).

However, non-local energy dissipations have been seen in numerical simulations by Ricker and Taam (2008) and Passy et al. (2012) during the rapid spiral-in phase. Ongoing domination of these effects after the rapid spiral-in phase could prevent the system to reach a

self-controlled phase.

Termination of controlled spiral-in

Two causes for the termination of the controlled spiral-in phase are possible. Either the envelope is ejected or the secondary fills its Roche lobe and mass transfer from the secondary takes place (e.g. Podsiadlowski, 2001; Ivanova et al., 2013). This might lead to the merger of the stellar cores.

Post–CE evolution

Further evolution of the post–CE system is expected. The formation of a fall-back disk could reduce the orbital separation of the binary (Kuruwita et al., 2016). The primary remnant might contract (Iben and Livio, 1993) and general thermal evolution of the stellar remnants could restart mass transfer (Ivanova et al., 2013).

2.3.2 Physical description of CE evolution

Historically, the first descriptions of close binary systems taking into account a common envelope equated the change in orbital energy E_{orb} due to the spiral-in with the binding energy of the envelope E_{bind} (e.g. van den Heuvel, 1976; Paczynski, 1976; Webbink, 1984; Livio and Soker, 1988). This approach is called the energy formalism.
Another approach introduced by Nelemans et al. (2000), which is called γ formalism, is based on the calculation of the angular momentum budget.

Energy formalism

The energy budget can be written as

$$\frac{GM_1 M_{env}}{\lambda a_i r_L} = \alpha_{CE} \left(\frac{GM_{1,c} M_2}{2a_f} - \frac{GM_1 M_2}{2a_i} \right) \tag{2.9}$$

(Dewi and Tauris, 2000) where a is the binary separation, subscripted with i and f for initial and final value, accordingly. $M_{1,c}$ is the mass of the primary after it lost its envelope of mass M_{env}. λ

is a numerical factor, called binding energy parameter, introduced by de Kool (1990) in order to account for different density distributions of the donor star. de Kool (1990) approximates λ by 0.5. Nowadays it is widely accepted that λ varies depending on stellar mass and evolution. For a recent study on the binding energy parameter see Wang et al. (2016). The efficiency parameter α_{CE} (named η_{CE} in Dewi and Tauris (2000)), introduced by Livio and Soker (1988), accounts for the efficiency with which orbital energy is used to drive off the envelope. It is defined as

$$\alpha_{CE} \equiv \frac{\Delta E_{bind}}{\Delta E_{orb}} \tag{2.10}$$

The value of α_{CE} remains uncertain. Effects that might influence the efficiency of energy deposition are e.g. efficient energy transport and nonspherical effetcs like mass ejection (Iben and Livio, 1993). If further energy sources, e.g. nuclear energy, help driving off the envelope it is also possible to get values of $\alpha_{CE} \gg 1$. Han et al. (1995) introduce the parameter α_{th} as efficiency parameter for the thermal energy. For their simulations they combine values of 0.0, 0.5 and 1.0 for α_{th} and 0.3 and 1.0 for α_{CE}. More recent results from Han et al. (2002) propose the values $\alpha_{CE} = \alpha_{th} = 0.75$ as the best solution to fit observations of subdwarf B stars in binaries.

γ formalism

In order to explain the evolution of observed systems of double white dwarfs in close orbits which underwent a CE phase and lost the envelope without a spiral-in phase Nelemans et al. (2000) brought forward the γ formalism. This should, according to Nelemans et al. (2000), be applied to systems with low mass ratio.
The essential equation is given in eq. 2.11. It is based on the assumption that the envelope is completely expelled and that the angular momentum of the systems is reduced linearly.

$$J_i - J_f = \gamma J_i \frac{\Delta m}{M} \tag{2.11}$$

The angular momentum is given by J, the indices chosen according to the energy formalism. As before, M is the sum of the stellar masses and Δ m is the total change of mass. Nelemans et al. (2000) estimate the value of γ for their observed systems to lie between ~ 1.4 and 1.85.

Advantages and disadvantages of the formalisms

For historical reasons, the energy formalism is more widely distributed and more often used than the γ formalism. This leads to the advantage that the parameters of the energy formalism are constantly under investigation and the formalism itself is improved (e.g. Zorotovic et al., 2014; Nandez and Ivanova, 2016; Wang et al., 2016).

Furthermore, there are indications that the energy formalism is more appropriate in order to describe the observed abundances of classes of systems (e.g. Zorotovic et al., 2010; Zuo and Li, 2014). The γ formalism is efficient in reconstructing the double helium WD systems for which it was originally introduced.

2.3.3   Remnants of CE systems

Common envelope evolution is one way how close compact binary systems form. The remnant systems of CE evolution are e.g. WDMS binaries (Rebassa-Mansergas et al., 2007), cataclysmic variables (CVs) (Kalomeni et al., 2016), high-mass X-ray binaries (Zuo and Li, 2014) as well as black-hole binaries and long-duration gamma ray bursts (Podsiadlowski et al., 2010). Further objects that experienced a CE phase are e.g. Type Ia supernovae (Iben and Tutukov, 1984; Kashi and Soker, 2011).

The wide variety of systems to which CE evolution can be applied is the reason why the detailed study of its physics is so important.

2.3.4   Numerical simulations of PCEB dynamics

Numerous studies on the impact and outcome of CE evolution have been published over the last decade. Here, I present a short and incomplete overview of the work of other scientists.

A high percentage of the published studies focuses on the second phase of CE evolution, namely the rapid inspiral. Among these are Ricker and Taam (2008, 2012). The authors analyze in particular the duration of the inspiral, the evolution of the orbital separation, the effect of drag forces on the secondary star and the resulting density distribution of bound and unbound gas. For this study, the authors use the grid-based adaptive mesh refinement (AMR) code FLASH[1]

---

[1]http://flash.uchicago.edu

(Fryxell et al., 2000; Dubey et al., 2008). A similar study of the spiral-in phase comparing two different numerical codes was carried out by Passy et al. (2012). Here, a comparison between the AMR hybrid code *Enzo* (O'Shea et al., 2004), combining N-body and hydrodynamics, and the Lagrangian smoothed-particle hydrodynamics (SPH) code SNSPH (Fryer et al., 2006) is drawn. I will review these three papers with more detail in succeeding paragraphs.

A comparable analysis is done by Ohlmann et al. (2016a) using the moving-mesh code *AREPO*. The strength of the code is the high spatial resolution that can be achieved. This enables the authors to observe the prominence of large-scale flow instabilities. Nandez and Ivanova (2016) use the SPH code *StarSmasher* to analyze the inspiral of a double white dwarf binary. The authors pay special attention to the effect of recombination energy on the outcome of the simulations with the result that including recombination energy decreases the mass that remains bound to the system. In Iaconi et al. (2017) the idea and setup of Passy et al. (2012) is picked up using the *Enzo* code. The authors investigate the outcome of the rapid inspiral under a wider initial separation of the binary. Furthermore, they compare these simulations with SPH simulations using *Phantom*. Iaconi et al. (2017) conclude that a wider initial separation results in a wider final separation because of the stellar expansion of the primary with differences not larger than 10% depending on the different codes. Ohlmann et al. (2016b) present the first magnetohydrodynamics simulations of the rapid spiral-in phase as an extension to Ohlmann et al. (2016a). The simulations show an amplification of magnetic fields during the inspiral. Nevertheless, the magnetic field strength is dynamically insignificant for the evolution of the binary. A set of Monte Carlo simulations was performed in Camacho et al. (2014) with the aim to better constrain the values of physical parameters of CE evolution by comparison with observations. As reference observations/ data the authors choose the set of WDMS binaries in the Data Release 7 of the Sloan Digital Sky Survey (SDSS)[2]. Camacho et al. (2014) introduce the parameter α_{int}, which is based on α_{th} as in section 2.3.2. The new notation, however, represents the inclusion of radiation and recombination energy. In general, the PCEB sample can be well reproduced with small values of α_{CE} and α_{int} and using a variable binding energy parameter. Finally, Kuruwita et al. (2016) set up simulations to form a fall-back disk based on Passy et al. (2012) using *Enzo*. The authors conclude that a disk helps reducing the final orbital separation of the binary, however, further energy sources are still required to help unbinding the envelope gas.
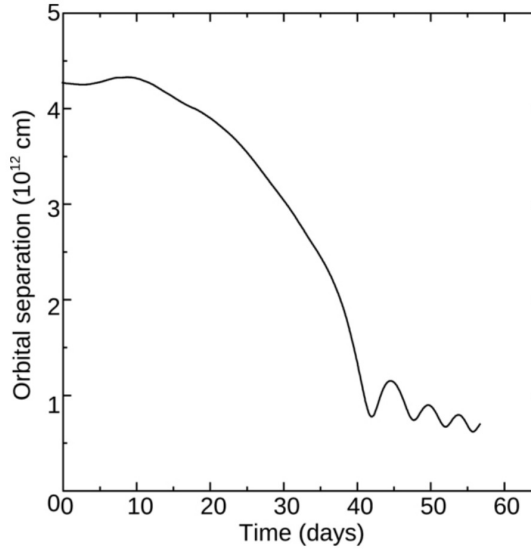
---

[2]www.sdss.org

Figure 2.6: Orbital separation of the binary plotted over time. The initial separation is 4.3×10^{12}cm. The decrease during the first 41 days is dominated by gravitational drag (Ricker and Taam, 2008). Figure from Ricker and Taam (2012).

Ricker and Taam

In the publications Ricker and Taam (2008) and Ricker and Taam (2012) (hereafter Paper I and II) the authors analyze the evolution of a $1.05\mathrm{M}_\odot$ red giant star with a core mass of $0.36\mathrm{M}_\odot$ and a $0.6\mathrm{M}_\odot$ companion. The red giant is modelled via a one-dimensional stellar evolution code and linearly interpolated onto a three-dimensional Eulerian mesh to be used in FLASH 2.4. The core of the red giant is subsequently substituted by a spherical particle cloud containing 200.000 Lagrangian particles moving as a solid body. Similarly, the secondary is represented by a spherical cloud of 200.000 Lagrangian particles within 6×10^{10} cm. The orbital period of the binary is 44.2 days at a separation of 4.3×10^{12} cm. The model of the primary is evolved for a dynamical timescale before the secondary is added. The stars are given circular orbital velocities and spin angular velocity. The simulation box of 4×10^{13} cm in each dimension is filled with ambient gas at a density of $10^{-9}\mathrm{g\ cm}^{-3}$ and pressure identical to the pressure of the outermost layer of the primary star. The evolution of the system is then followed for a total of 56.7 days. The analysis of the first 41 days is presented in Paper I, the end of the simulation is presented in Paper II. Figure 2.6 shows the evolution of the orbital separation of the binary over time. The inspiral starts after about 27 days. At the end of the simulation the orbit is still decaying with a timescale of about 35 days. The periastron separation has decreased to $\sim 6 \times 10^{11}$ cm. The gas density distribution in the vicinity of the stars after 56.7 days is plotted in Fig. 2.7 along with the velocity
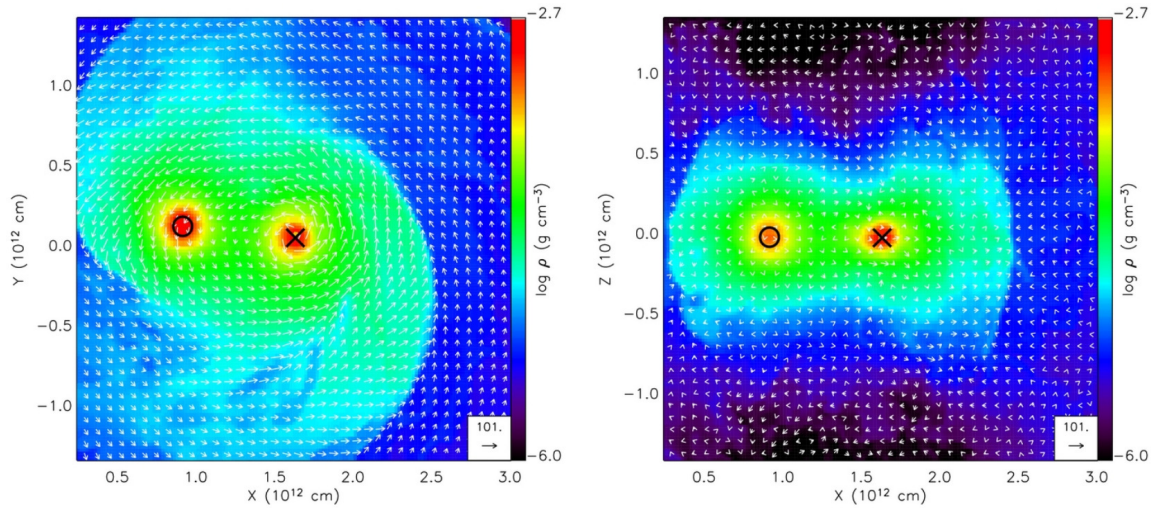
Figure 2.7: Velocity field ($\mathrm{km\ s^{-1}}$) and density distribution after 56.7 days of evolution. The location of the core is represented by $\times$, $\circ$ represents the companion star. Left: xy-plane, right: xz-plane. Ricker and Taam (2012).

field. The image shows that the gas rotates around the companion almost spherically symmetric in the xy-plane, the red giant core orbits along with the gas. In the xz-plane, the gas density distribution is flattened along the z-axis, resulting in a toroidal structure. The density distribution on larger scales along with radial profiles of gas density, pressure and radial as well as tangential velocity is shown in Fig. 2.8. The vertical lines in the radial profiles at the positions of jumps in the parameters clearly correspond to the spiral features visible in the gas density distribution. These features are characterized as spiral shocks.

Finally, the amount of unbound gas, displayed in Fig. 2.9, is $0.18\mathrm{M_\odot}$ at the end of the simulation. This is about 26% of the total envelope mass.
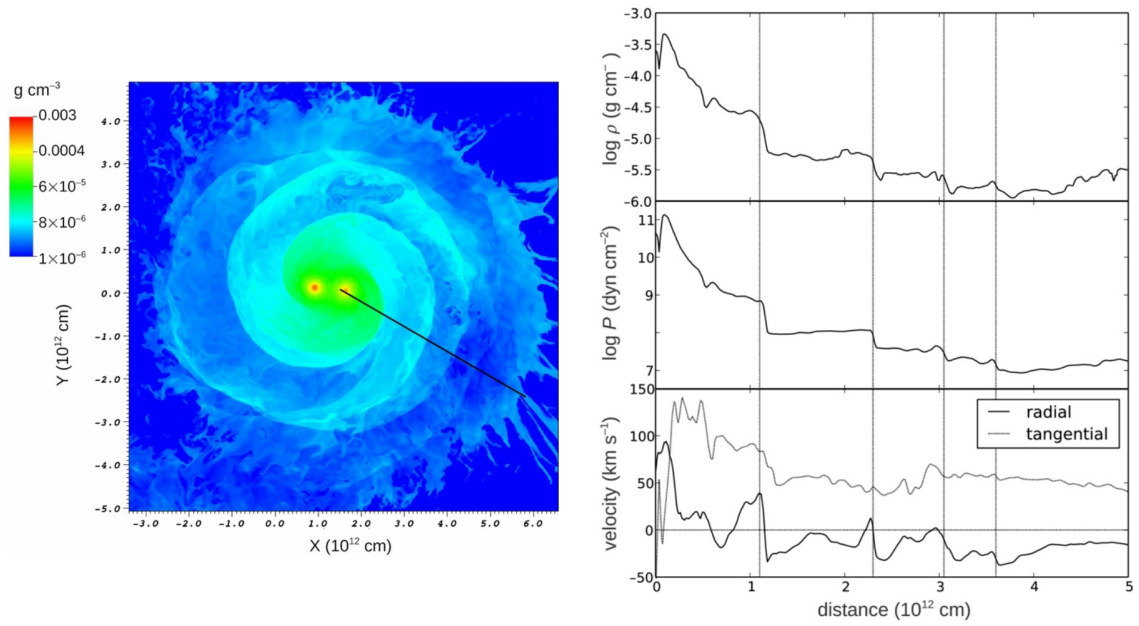
Figure 2.8: Left: density distribution in the xy-plane after 56.7 days. The black line indicates the direction for radial profiles plotted on the right. Right: Radial profiles of density, pressure, radial and tangential velocity (top to bottom) after 56.7 days. Vertical lines indicate the positions of spiral shocks. Ricker and Taam (2012).
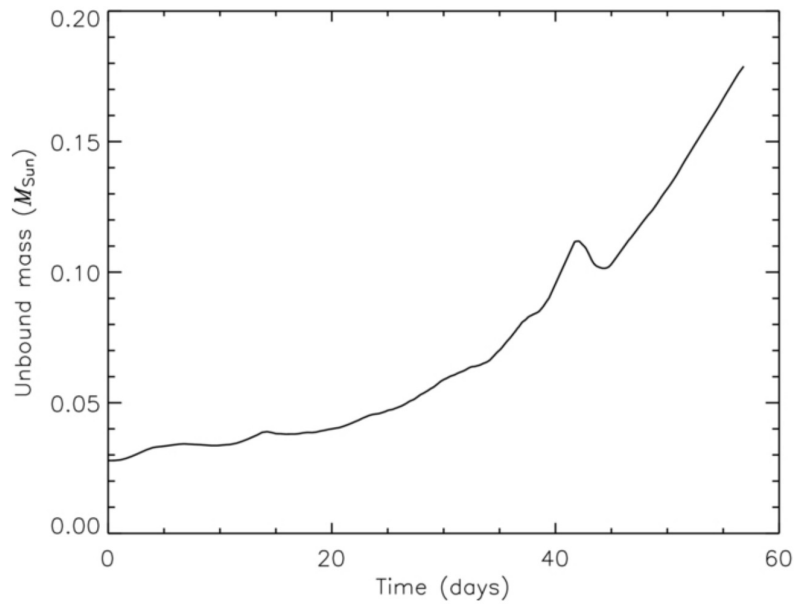

Figure 2.9: Unbound mass from Ricker and Taam (2012). The final amount of ejected mass is $0.18\mathrm{M_\odot}$. At the beginning a fraction of $0.03\mathrm{M_\odot}$ is already unbound.

Passy

Passy et al. (2012) investigate a series of simulations comparing different initial conditions and two different numerical codes. A detailed analysis is given for three simulations, the main parameters of which are summarized in Table 2.1.

Name	N_{part} or N_{cells}	$M_2(M_\odot)$	$A_0(R_\odot)$	$P_0(days)$	v_0/v_{circ}	$A_f(R_\odot)$	$P_f(days)$
SPH2	500,000	0.6	83	72	1	20.6	10.1
Enzo2	128^3	0.6	91	83	1	20.0	11.0
Enzo7	256^3	0.6	85	75	1	19.2	9.8

Table 2.1: Main parameters of three selected simulations. N_{part} or N_{cells} is the number of particles or cells used for the simulation, M_2 is the secondary mass, A_0, P_0 (A_f, P_f) denote the initial (final) orbital separation and period, v_0/v_{circ} is the orbital velocity of the secondary given in terms of the Kepler velocity.

The primary star is based on a one-dimensional model of a $1M_\odot$ MS star evolved to the RGB phase. The density profile is achieved in the SPH simulations by adding particles around a core particle with mass M_c and requesting smooth connections at the boundary between core and envelope. The pressure profile is determined by the initial value at the boundary and the assumption of hydrostatic equilibrium.

For simulations with *Enzo* the one-dimensional stellar model is used to define a spherically symmetric three-dimensional primary, the core is represented by a point mass. The simulation box of size 3×10^{13} cm is filled with ambient medium of constant density. As was done in the simulations in section 2.3.4, the setup is evolved for a few dynamical timescales before the secondary, represented by a point mass, is added. All simulations are run for 1000 days.

The evolution of the orbital separation of the binary over time for the Enzo7 simulation is shown in Fig. 2.10. Compared to Ricker and Taam (2012) the infall phase starts at a similar time after the beginning of the simulation. However, the separation decays slower.
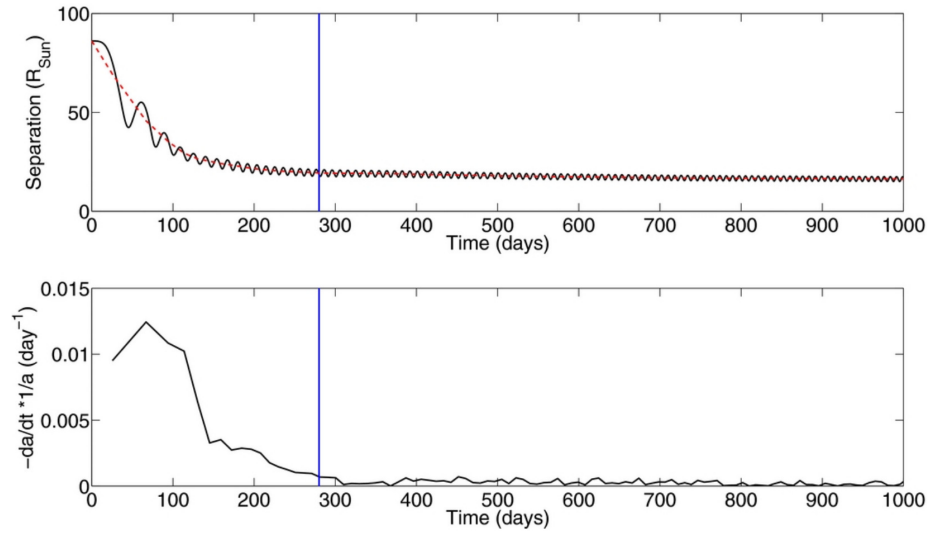
Figure 2.10: Top: orbital separation of the binary plotted over time. Bottom: orbital decay averaged over each cycle (top, red dashed line). The location of the blue vertical line shows the defined end of the rapid spiral-in phase. Image from Passy et al. (2012).

For the same simulation, the gas density distribution and velocity field can be compared to Ricker and Taam (2012) (see Fig. 2.11). After 50 days (Fig. 2.11, second row) the distribution in the xz-plane (right) appears similar to the distribution in Fig. 2.7. The evolution of spiral shocks detectable via radial profiles as in 2.8 (bottom) as well as a uniform flow pattern occur later, visible after 85 days (Fig. 2.11, third row).
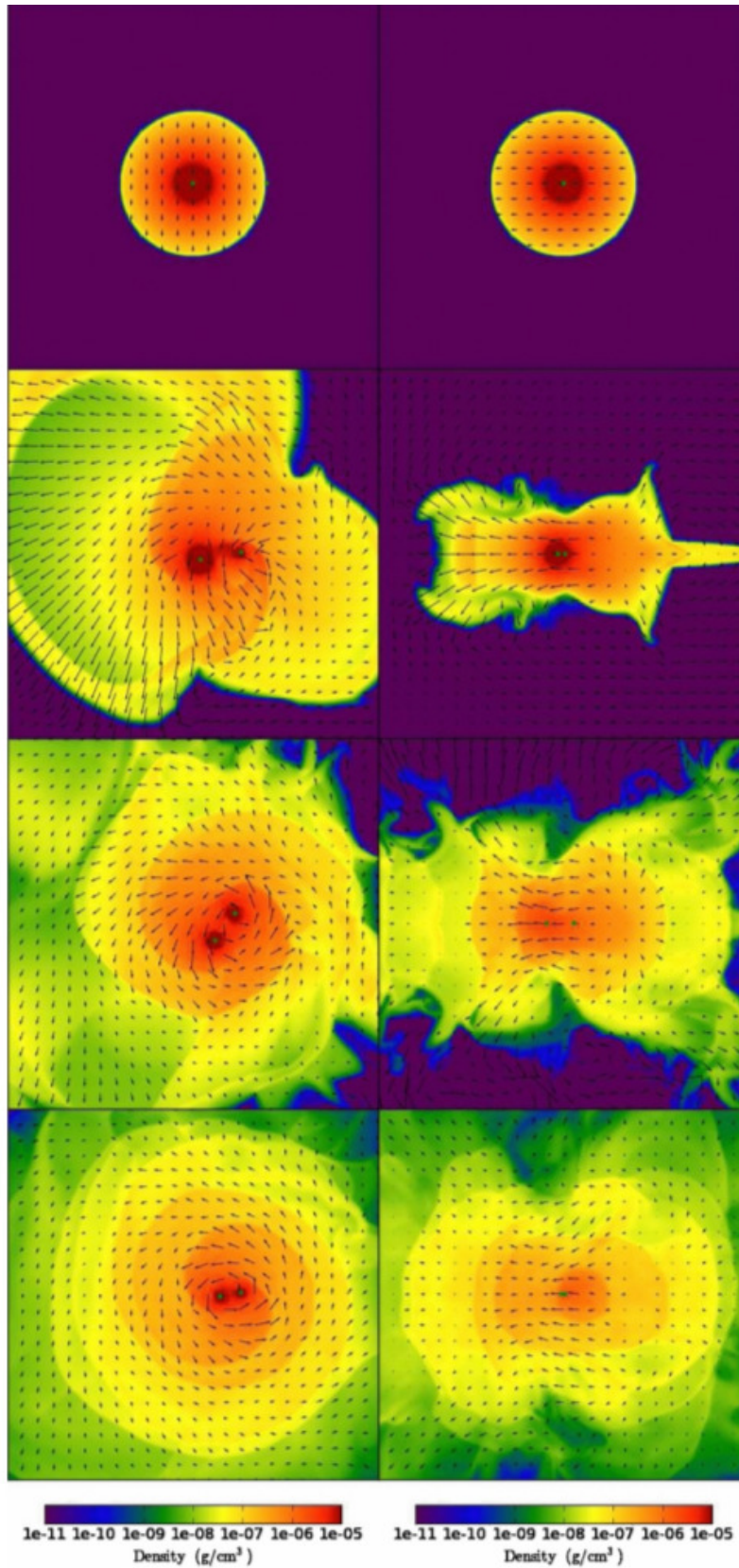
Figure 2.11: Gas density distribution and velocity field (scaled to $23\,\mathrm{km\,s^{-1}}$ in top panel) in the xy- (right) and xz-plane (left) for Enzo7. The evolution is shown after $0, 50, 85$ and 130 days (top to bottom). Passy et al. (2012).
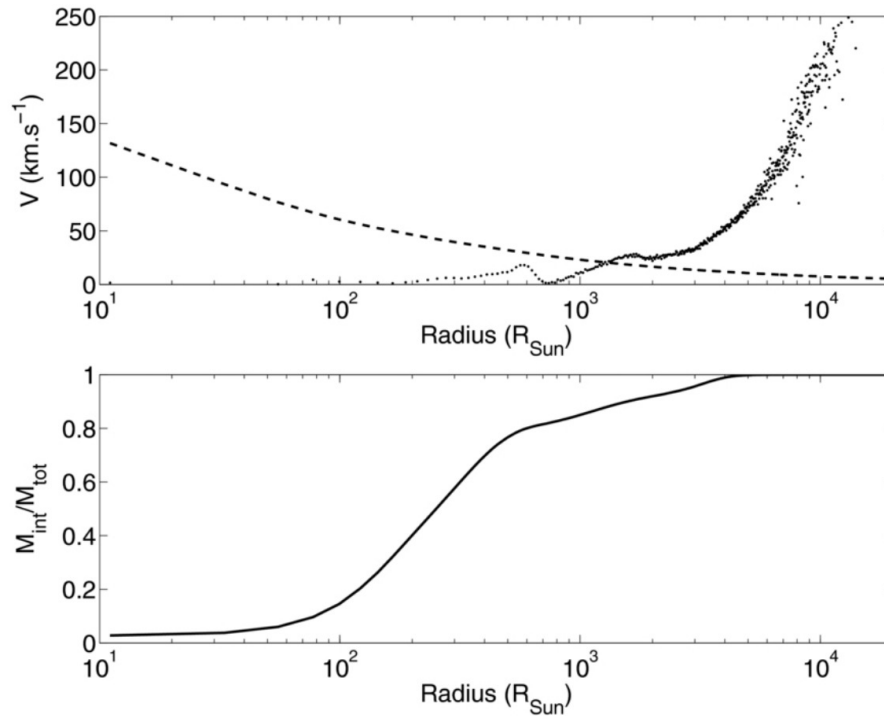
Figure 2.12: Top: escape velocity (dashed line) and radial velocity (black dots) of the gas plotted over radius at the end of the SPH2 simulation. Bottom: enclosed mass over radius. Passy et al. (2012).

The unbound mass in the SPH2 simulation is less than 15% of the envelope mass as can be deduced from Fig. 2.12. The unbound gas is at radii larger than $10^3 R_\odot$.

For the SPH2 simulation, Passy et al. (2012) plot a detailed analysis of the evolution of the energy components. This is shown in Fig. 2.13. At the beginning of the simulation, during the inspiral, the internal energy of the system (U_{tot}, green dashed line) and the orbital energy of the core and companion (E_{c2}, black dashed line) decrease while the envelope expands, Φ_{env} (blue dashed line) increases. After the inspiral (> 280 days), the values of the energy components remain almost constant.
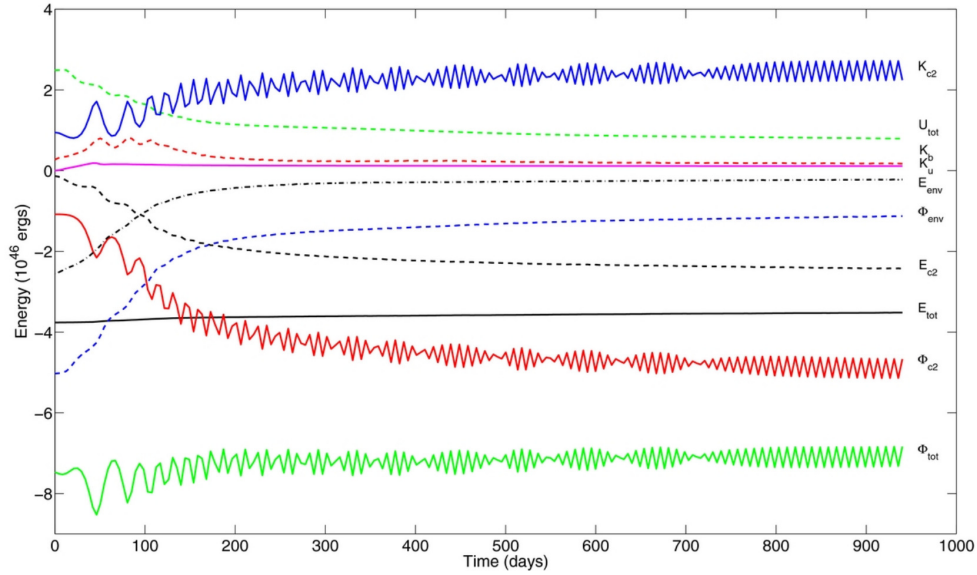
Figure 2.13: Evolution of the energy components for the SPH2 simulation of Passy et al. (2012). The total energy E_{tot} is plotted as black line. The gravitational potential energy Φ of the system (indexed tot), the envelope (indexed env) and the core and companion (indexed c2) are plotted as well as the kinetic energy K of the core and companion, the bound mass (indexed b) and the unbound mass (indexed u), the internal energy of the system U_{tot}, the total energy of the envelope E_{env} and the orbital energy of the core and companion E_{c2}. Total energy is conserved up to more than 10%.

Conclusion on numerical studies

The presented studies show that the CE phase is not well constrained. The parameters of the system after the infall phase, e.g. the remaining bound mass and the radial velocity of the gas, strongly depends on the initial conditions. These are determined by the stellar masses and the mass of the envelope as well as the total energy of the system. Therefore, a parameter study is necessary in order to numerically study the post–CE phase.
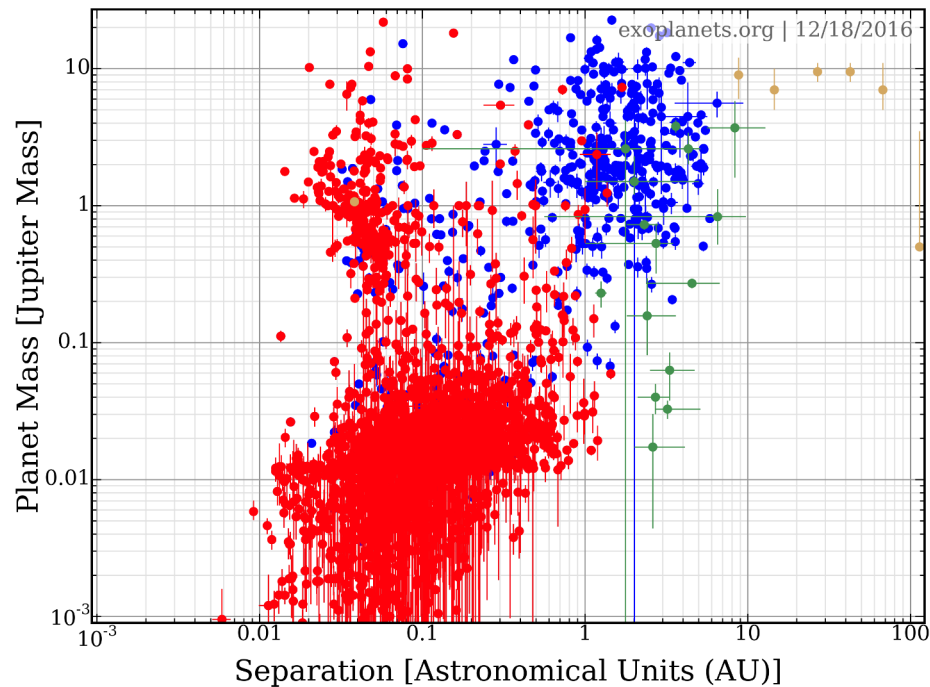
Figure 2.14: Planet mass versus planet separation in double logarithmic scale. The planets are colour coded by detection method. Blue: radial velocity, red: transit, green: microlensing, yellow: direct imaging.

2.4   Extrasolar planets

The first detection of a planet outside our own solar system around a solar-type star was reported in 1995 by Mayor and Queloz (1995). 51 Peg b is a Jupiter-mass planet with orbital distance of 0.05 AU (see exoplanets.org and Han et al. (2014)) to its host star. Since 1995 the number of detected planets has increased by thousands. Fig. 2.14 shows an overview of the distribution of announced exoplanets by December 18, 2016 by the Exoplanet Data Explorer at exoplanets.org. To this date, the Exoplanet Data Explorer lists 2950 confirmed planets.

 The planets in Fig. 2.14 are colour coded by detection method. The most common detection methods are described in the following.

Radial Velocity

Due to the gravitational force of a planet its host star moves around the common center of mass. Unless the orbit is observed exactly face on the star will be moving in the radial direction with respect to the observer. This radial motion can be observed via spectroscopy as a shift to the red

or blue in the spectrum for the star moving away or coming towards the observer, respectively. The extent of the Doppler shift is larger for massive planets in close orbits. With the radial velocity (RV) method it is possible to determine a mass limit of the planet depending on the inclination angle i ($i = 0°$ for face on view, $i = 90°$ for edge on view) as $m \cdot \sin(i)$.

The planets detected via RV are the blue circles in Fig. 2.14.

Transit

The transit of a planet in front of its host star decreases the observed stellar flux. The transit depth depends on the diameter of the planet. A typical value for the transit depth in terms of $R_{\mathrm{planet}}/R_{\mathrm{star}}$ is 10^{-4} to 10^{-3}. The frequency of a transit depends on the orbital distance of the planet to the star. Therefore, the detection probability increases with decreasing separation.

The planets detected via transit are the red circles in Fig. 2.14. A large number of these planets were discovered by the Kepler mission which was specifically designed in order to detect Earth-size planets in the Milky Way (Borucki et al., 2008).

A combination of transit and RV measurement is of very high interest because it allows to determine the density of the planet.

Microlensing

The idea of gravitational lensing dates back to Einstein (1936). If the light of a background source passes a massive object (lens) it will be deflected due to gravity. Depending on the geometrical conditions the observer might see multiple images of the source or one distorted image. In any case, the apparent brightness of the source increases. In the case of a single star acting as lens on a single background star, a microlensing event, the observed intensity of the source star shows a symmetrical variation. A stellar lens with a planetary companion however would lead to an asymmetrical variation of the lightcurve and thereby reveal the presence of the companion. This detection method is sensitive to massive planets at moderate distances of a few AU (Ollivier et al., 2009).

The planets detected via microlensing are the green circles in Fig. 2.14.

Direct Imaging

Direct imaging is photometry of the planet. It is influenced by the contrast and distance between planet and star, i.e. the method is biased towards detecting massive planets with large

separations.

The planets detected via direct imaging are the yellow circles in Fig. 2.14.

Extrasolar planets are also detected in stellar binaries or multiple stellar systems. The number of planets in these kind of systems listed in the Exoplanet Data Explorer by June 2017 is 680. A detection method, applicable for planets in eclipsing binary systems, is the light-time effect.

Light-time effect

For an eclipsing binary system it is possible to determine the epoch of minimum of an eclipse very precisely. In a tight, undisturbed system the eclipse should occur periodically with a constant period T. In the case of a planet orbiting an eclipsing binary the motion of the binary around the center of mass of the three-body system leads to a shift of the binary in the direction towards and away from the observer once per orbital period of the planet. With the increased (decreased) distance between the binary and observer the eclipses are observed later (earlier) compared to the undisturbed binary system. This is the light-time (LTT) effect. The difference between observed timing and calculated timing of the undisturbed system can be plotted in a so called O-C diagram. If a single planet is in circular orbit around the eclipsing binary the O-C diagram displays cyclic changes.

Note that the occurence of cyclic changes in the O-C diagram is not a proof for the existence of a third body orbiting the eclipsing binary.

A list of observed eclipsing PCEBs showing variations in the O-C diagram is given in Zorotovic and Schreiber (2013). This list also includes the system NN Serpentis (NN Ser).

2.5   NN Serpentis

The binary system NN Serpentis (ab) consists of a white dwarf and M dwarf. Precise measurement of the parameters is given in Parsons et al. (2010). The white dwarf has a mass of $M_{WD} = 0.535 \pm 0.012 M_\odot$ and radius of $R_{WD} = 0.0211 \pm 0.0002 R_\odot$. The values for the M dwarf are $M_{sec} = 0.111 \pm 0.004 M_\odot$ and $R_{sec} = 0.149 \pm 0.002 R_\odot$. The temperature of the WD is given by 57000 ± 3000 K (Haefner et al., 2004). The binary separation is determined to be $a_f = 0.934 \pm 0.009 R_\odot$. Beuermann et al. (2010) estimate the mass of the WD progenitor $\sim 2 M_\odot$ and the initial separation of the binary $a_i \sim 1.5$ AU. The period of the system is P = 0.130 d (Brinkworth et al., 2006). The authors also detect a period decrease of $\dot{P} = (9.06 \pm 0.06) \times 10^{-12} \text{s s}^{-1}$.

Among other explanations for the period change in binary systems is the Applegate mechanism (Applegate, 1992). In this model, Applegate proposes that a reallocation of angular momentum within an active star during its activity cycle leads to a change in the oblateness of the star and therefore to a change of its quadrupole moment. The variation of the quadrupole moment affects the gravitational acceleration and thereby causes a change in the orbital period. Brinkworth et al. (2006) calculate the energy budget for NN Serpentis and resume that the available energy is too low to explain the observed period moduliations by Applegate's mechanism.

Further mechanisms explaining the observed ecplipse variations, e.g. apsidal motions (Parsons et al., 2014), are ruled out as well, thus only leaving the existence of planetary companions as trigger.

The system was proposed to harbor two planets by Beuermann et al. (2010) using the LTT effect. A plot of the O-C mid eclipse time differences relative to a two-planet model is shown in Fig. 2.15.

The planetary masses as determined in Beuermann et al. (2013) are $7.0 M_J$ and $1.7 M_J$. The semi-major axis of the planetary orbit is 5.4 AU and 3.4 AU, respectively. The planetary solution was tested for dynamical stability (Beuermann et al., 2013). Although there is no confirmation for the existence of the planets I will adopt the phrasing of *planets* instead of *planet candidates* in the following.

The origin of the planets is not clear at all. Either they are first-generation planets, i.e. they were formed before the binary evolved into a PCEB, which experienced a dramatic change in system parameters during and after the CE phase. Or they are second-generation planets which
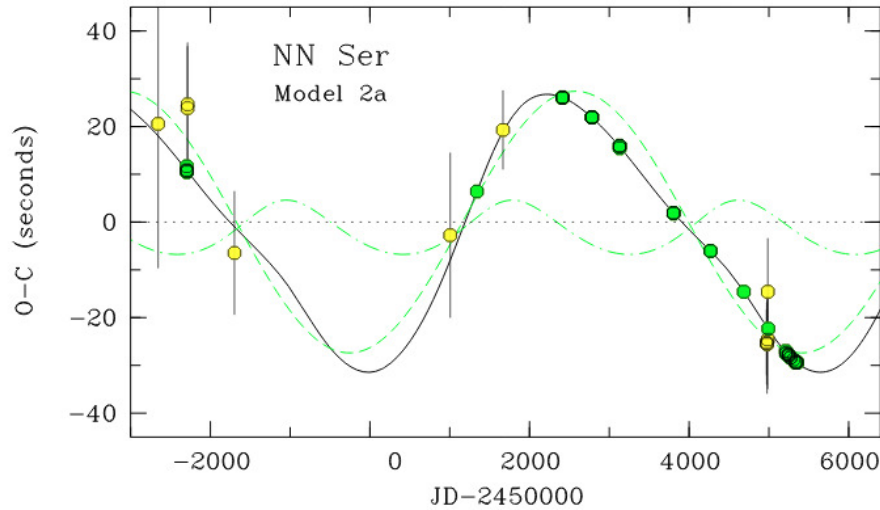
Figure 2.15: O-C mid eclipse time differences as yellow and green dots representing data points with errors > 1s and < 1s, respectively. Overplotted in green are the contributions of components b and c by dashed and dot-dashed lines, respectively, to the best-fit model plotted as black solid line. Figure from Beuermann et al. (2010).

formed out of a fall-back disk after the CE phase. In the latter case, the planets' age would be restricted by the white dwarf cooling age to be less than 1 Myr (Beuermann et al., 2010).

Since NN Serpentis is unique in the sense that the hypothesis of the existence of planets persists even after many years of observations I will base the basic parameters of my simulations on the parameters of this system.

I will summarize the results of Völschow et al. (2014) and Schleicher et al. (2015) which argue against a first-generation and for a second-generation scenario in section 2.5.1 and 2.5.2, respectively.

2.5.1 Analytic examination of first-generation planets

In Völschow et al. (2014) the authors investigate the effects of a change in the gravitational potential of a binary star on orbiting planets. This is a simple model for a mass-ejection event, neglecting any further effects on the system. The authors examine two different cases depending on the mass loss timescale τ and the planet's orbital period P_i:

1. adiabatic mass loss with $\tau \gg P_i$

2. instantaneous mass loss with $\tau \ll P_i$

Considering NN Serpentis with a mass-loss factor $\mu = M_f/M_i \approx 0.3$ and the planets on circular orbits with initial semi-major axes > 3.5 AU (Beuermann et al., 2010) the planets would

1. have final semi-major axes > 10 AU; or starting at the final positions as published by Beuermann et al. (2013) the planets initial semi-major axes had to be < 2 AU which leads to dynamically unstable orbits in the initial system.

2. reach escape velocity and get ejected.

Considering initially elliptical orbits

1. all orbital parameters of the planets would be conserved, i.e. $P_i = P_f$ etc.

2. the final eccentricity and semi-major axis depend on the distance r_i and polar angle ϕ_i of the planet at the moment of mass ejection.

Evaluating these conditions for NN Serpentis, Völschow et al. (2014) conclude that adiabatic mass loss is excluded for typical CE events with $\tau \ll P_i$ and instantaneous mass loss would require initial eccentricities $e_i \approx 0.4$, see also Fig. 2.16 for escape probabilities depending on initial eccentricity, which again makes it difficult to find stable solutions for the initial planetary system.

Furthermore, the authors investigate the effect of geometric gas drag effects on the mass-loss event. They show that as well for the spherical symmetric case as for a disk-shaped case of mass-ejection the geometric gas drag can be neglected. Therefore, the results shown above require a second-generation planet scenario for the system NN Serpentis.

2.5.2   Second-generation planet formation

The formation of a disk from fall-back material can be modeled under the assumption of a specific ejection scenario. To do so, Schleicher and Dreizler (2014) adapt a model for the ejection event from Kashi and Soker (2011). In addition to the known physical values from NN Ser the authors assume a power-law density profile for the envelope and the case that the ejection occurs when the released gravitational energy from the binary, E_{orb} in the notation of 2.3.2, exceeds the
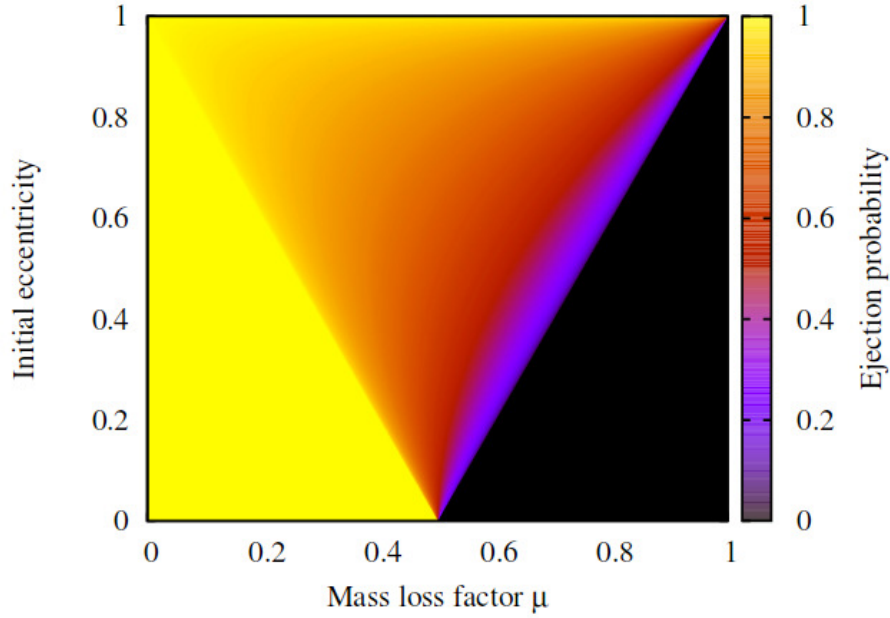
Figure 2.16: Considering instantaneous mass loss, this figure shows the escape probability of a planet depending on its initial eccentricity and the mass loss factor of the system. Fig. 1 from Völschow et al. (2014).

binding energy of the envelope (E_{bind}). However, parts of the gas mass outside the radius where $E_{bind} = E_{orb}$ might not reach escape velocity but stay gravitationally bound to the system and form a disk. To estimate the fraction of gas mass that does not leave the system, the authors apply a model by Kashi and Soker (2011) in order to determine the post-shock velocity profile of the gas. For NN Ser, Schleicher and Dreizler (2014) find a remaining gas mass of $\sim 0.133\,\mathrm{M_\odot}$. To derive the mass available for disk formation the parameter α_M is introduced which accounts for corrections of the gas mass due to the underlying assumptions. The potential disk mass is then

$$M_{disk} = \alpha_M M_{bound}. \tag{2.12}$$

Assuming this gas forms a fall-back disk described by a power-law profile of the gas surface density $\Sigma(r) = \Sigma_0\left(\frac{r_{out}}{r}\right)^n$, where r_{out} is the outer radius of the disk and Σ_0 the surface density of the disk at r_{out}, with n = 1 and efficient cooling of the disk due to dust, the Toomre Q parameter, given by

$$Q = \frac{c_s \Omega}{\pi G \Sigma} \sim 1, \tag{2.13}$$

will decrease. Here, c_s denotes the sound speed and Ω is the rotation under the assumption of Kepler rotation around an object with the same central mass as the present system. Following e.g. Boley et al. (2010), the authors estimate the mass of initial clumps forming by gravitational instabilities (GI) to be

$$M_{cl} = \Sigma(r)h^2(r) \tag{2.14}$$

with h being the disk height. The upper limit for the final mass of the clumps that can be reached, delimited by the formation of a gap, is

$$M_f = M_{cl}\left[12\pi\frac{\alpha_{crit}}{0.3}\right]^{1/2}\left(\frac{r}{h}\right)^{1/2} \tag{2.15}$$

where α_{crit} is the critical value for viscous dissipation.

Applying this model to NN Ser, Schleicher and Dreizler (2014) derive final masses for planets at 5.4 AU and 3.4 AU of $\sim 6.6\,\mathrm{M_J}$ and $\sim 1.9\,\mathrm{M_J}$, respectively. These values are remarkably close to the observed system.

In addition, the authors point out the possibility that first-generation planets could accrete mass from the disk to form the observed system NN Ser, a scenario that is not ruled out by Völschow et al. (2014). The formation of planets through core accretion however seems rather unlikely due to the young age of NN Serpentis.

3

Numerical Hydrodynamics

For the work presented in this thesis I make use of the FLASH code, version 4.2.2, with an additional gpu implementation published in Lukat and Banerjee (2016).

In section 3.1 I give a short introduction to FLASH. Subsequently, I explain the fundamental setup which is used for the simulations in section 3.2.

3.1 FLASH

FLASH is a finite-volume adaptive mesh refinement (AMR) code (Berger and Colella, 1989), originally written for solving the hydrodynamic problem of nuclear flashes. It allows for user defined applications by a wide variety of compatible modules. These adress amongst others the solvers for hydrodynamics (HD), gravity and the equation of state, the grid solvers and the inclusion of Lagrangian particles.

The FLASH code is parallel using the Message Passing Interface (MPI).

The publication Fryxell et al. (2000) presents in detail the architecture of the code, the algorithms solving the hydrodynamics and thermodynamics as well as some test and benchmark cases.

In the following sections, I summarize some of the most important features for my simulations, namely the hydro- and thermodynamics algorithms, the adaptive mesh technique and sink particles.

3.1.1 Adaptive Mesh Refinement

I use the PARAMESH package (MacNeice et al., 2000) included in the FLASH code for setting up the adaptive grid.

PARAMESH is a block-structured AMR, i.e. it assumes a logically Cartesian order of blocks of cells where in three dimensions the neighboring cells in x-direction of the cell defined by grid point (i,j,k) are (i-1,j,k) and (i+1,j,k). FLASH only supports cell-centered data solutions. Thus, the coordinate triple (i,j,k) denotes the center point of the cell. Refining a block is accomplished by halving it along each dimension. In 3D simulations this results in a new subset of eight blocks. These children blocks have in sum exactly the same size as the parent block. The block structure is stored in a tree, see Fig. 3.1 for a 2D example. There exist several criteria for the refinement and derefinement of a block. One example is that neighboring blocks may not differ by more than one level in refinement.

Each block consists of eight interior cells surrounded by guard cells. The number of guard cells at each boundary is defined by the user. Here, I use a layer of four guard cells. The data solutions in the guard cells are copied from neighboring blocks unless the block is at a boundary of the computational domain. In that case the solution is calculated depending upon boundary conditions.
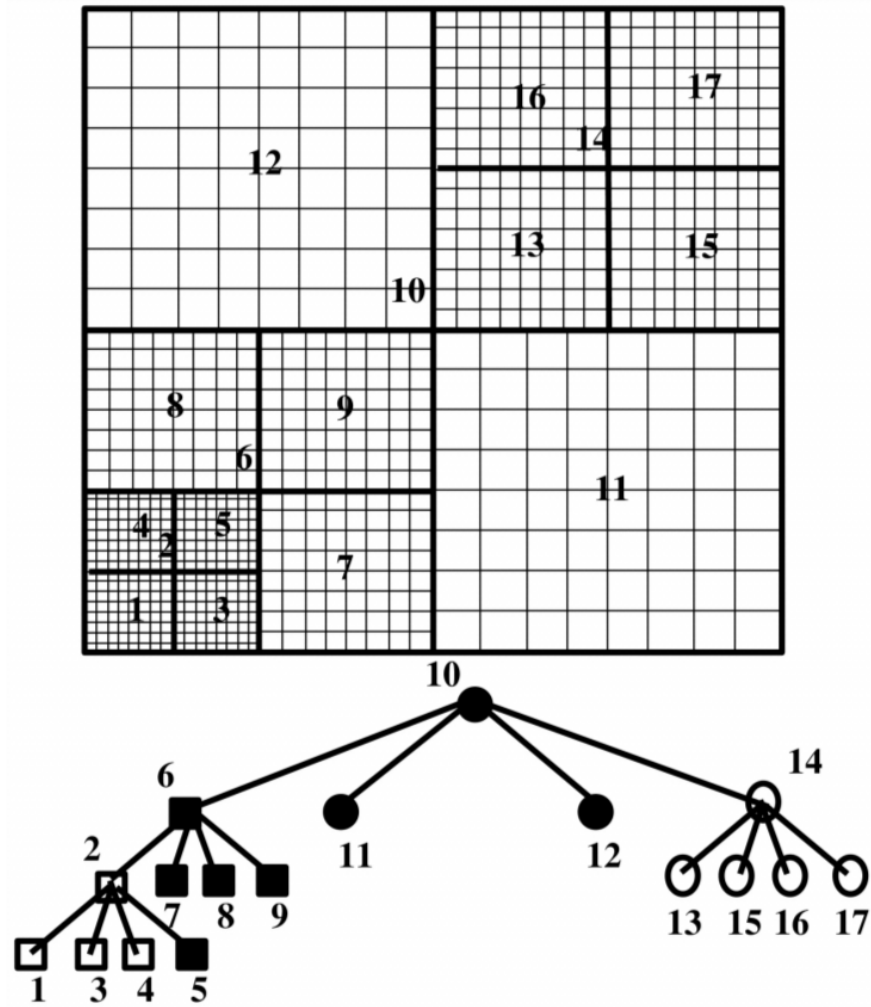
Figure 3.1: 2D grid with different levels of refinement related to tree structure. The block at refinement level 1, block 10, is split into blocks $6, 11, 12$ and 14. The highest level of refinement is reached for blocks $1, 3, 4$ and 5 with refinement level 4. The tree relates parent and children blocks. Figure from Fryxell et al. (2000).

3.1.2   Hydro- and Thermodynamics

In order to evolve the dynamics of the gas, FLASH solves the Euler equations. These are given in the conservative form in equations 3.1 - 3.3. Here, ρ and $\mathbf{v}$ denote the fluid density and velocity, respectively. P is the pressure and Φ is the gravitational potential. The energy E is the sum of internal energy $\rho\epsilon$ and kinetic energy, given by $E = \rho\epsilon + \frac{\rho}{2}|\mathbf{v}|^2$.

$$\frac{\partial\rho}{\partial t} + \nabla\cdot(\rho\mathbf{v}) = 0 \tag{3.1}$$

$$\frac{\partial\rho\mathbf{v}}{\partial t} + \nabla\cdot(\rho\mathbf{v}\mathbf{v}) + \nabla P = -\rho\nabla\Phi \tag{3.2}$$

$$\frac{\partial E}{\partial t} + \nabla\cdot[(E + P)\mathbf{v}] = -\rho\mathbf{v}\cdot\nabla\Phi \tag{3.3}$$

These three equations represent the conservation of mass (3.1), momentum (3.2) and energy (3.3) under the action of gravitational forces. The pressure is derived by solving the equation of state. For the study presented here this is a polytropic EOS with polytropic constant K and polytropic index Γ, given in equation 3.4. The gravitational potential Φ depends on the density ρ of the gas and is determined via the Poisson equation (equation 3.5).

$$P = K\cdot\rho^\Gamma \tag{3.4}$$

$$\nabla^2\Phi = 4\pi G\rho \tag{3.5}$$

The internal energy $\rho\epsilon$ and temperature T are calculated depending on pressure and density, resulting in $T \propto \rho^{\Gamma-1}$. I have chosen the polytropic EOS in order to avoid unphysical temperatures arising from the combination of the sink particle module and the gamma-law EOS module.

In order to update the values for the conserved variables in each time step one has to solve a Riemann problem for the discontinuity represented by the cell interfaces. This is done by the hydrodynamic solver. For this study, I use a solver implemented in FLASH as alternative magnetohydrodynamic (MHD) module by Waagan et al. (2011). In comparison to other available HD and MHD solvers this solver showed the best stability.

3.1.3   Sink particles

Sink particles are Lagrangian particles, i.e. they can move independently of the grid within the computational domain. Krumholz et al. (2004) were the first to use sink particles in grid-based AMR code. Federrath et al. (2010) implemented sink particles in FLASH.

Sink particles were originally supposed to represent bound regions of high density that are going to collapse in order to prevent the violation of the Truelove-criterion (Truelove et al., 1997). This criterion limits the resolution of the Jeans length in units of the cell size by which artificial fragmentation can be avoided. Thus, sink particles interact gravitationally with gas and are also able to accrete gas. Moreover, sink particles interact gravitationally with other sink particles. As in my simulations, sink particles can also be used to represent stars or planets. To do so, I initiate a sink particle at a pre-defined position with given mass and velocity. Calculated gravitational interactions in simulations are: sinks on sinks, sinks on gas, gas on sinks and gas on gas.

- *Gas on gas* interactions are solved using a Poisson solver. In my case this is a solver for the gpu implementation (Lukat and Banerjee, 2016).

- *Gas on sinks* interactions are calculated by interpolation of the gas-gas interaction at the position of each sink particle.

- *Sinks on gas* interactions are calculated via the sum over all sink particles for each cell, taking into account the masses of the sink particles and the corresponding distance to the cell center. In order to avoid accelerations approaching infinite values for particles close to cell centers a gravitational softening is applied within the pre-defined sink softening radius. The calculated acceleration is added to the gas-gas acceleration.

- *Sinks on sinks* interactions are calculated via the sum over all paricles, again taking gravitational softening into account. The result is added to the gas-sinks acceleration.

A time step for the evolution of sink particles is calculated, depending on several conditions. An upper limit for the sink particle time step is set by the hydrodynamic time steps, a lower limit

is set by considering the smallest distance between any two sink particles. Blocks containing sink particles are always on the highest level of refinement.

3.2   Setup for the performed simulations

In the following section, I describe the setup for my simulations. All terms that are used, such as α, from now on refer to simulation parameters.

    The envelope of the CE system is modeled as a gaseous sphere with given density and velocity distribution. It is surrounded by ambient medium at rest with density ρ_{amb} in a box with length of 40 AU in each dimension. Within the envelope I define a core with radius r_{core} and constant density ρ_0. Outside r_{core} the density decreases as $r^{-\alpha}$. The central density is determined by the total mass M_{env}. The total kinetic energy E_{kin} is split into two parts via the parameter *rad*. One part is the kinetic energy of the radial motion of the gas which increases proportional to $r^{0.5}$. The second part is the kinetic energy of the angular motion. The gas is set in rotation around the z-axis. With r_{cyl} being the distance to the z-axis the toroidal velocity decreases proportional to $r_{\mathrm{cyl}}^{-0.5}$.

Temperature, pressure and internal energy of the gas are calculated via the EOS.

    The solid objects in the system are represented by sink particles. One sink particle, $\mathrm{sink}_{\mathrm{bi}}$, represents the stellar binary. The mass of the binary as well as of the envelope is chosen such as to represent the system NN Serpentis as introduced in section 2.5. The sink particles $\mathrm{sink}_{\mathrm{p1}}$ and $\mathrm{sink}_{\mathrm{p2}}$ both represent a planetary object. All three sink particles are initiated at setup time with defined mass and velocity at fixed positions. Sink merging or accretion of gas onto sinks is not activated in the simulations.

All setup variables which stay fixed for the set of simulations are summarized in Tables 3.1 (gas) and 3.2 (sinks).

    Since the initial parameters during the CE phase for PCEB systems are not known I carry out a parameter study. Therefore, I define a parameter space of velocity distribution (rad), total kinetic energy E_{kin} and density slope α. The choice for the values of rad as well as for α are based on the results of Ricker and Taam (2012) and Passy et al. (2012). These simulations show that the gas is rotating at the end of the rapid infall phase and in both cases the density decreases with $\sim r^{-2}$ at the end of the simulations. In order to account for different initial conditions and to test various scenarios we choose values for rad of 0.5, 0.7 and 1.0 and α takes on the values 1, 1.5 and 2. I parametrize the total kinetc energy E_{kin} by the change in orbital energy ΔE_{orb} of

parameter		default value
total mass of the envelope	M_{env}	$1.5\,M_{\odot}$
radius of the envelope	R_{env}	1 AU
core radius	r_{core}	0.33 AU
density of the ambient medium	ρ_{amb}	$1.5 \cdot 10^{-15}\mathrm{g\,cm}^{-3}$
polytropic gamma	Γ	1.5

Table 3.1: Default values for the initial setup of the gaseous envelope and the ambient medium.

parameter	initial value		parameter	initial value		parameter	initial value	
m_{bi}	0.65	$M_{\odot}$	m_{p1}	2.1	M_J	m_{p2}	6.32	M_J
x_{bi}	0	AU	x_{p1}	3.5	AU	x_{p2}	-2.0	AU
y_{bi}	0	AU	y_{p1}	0	AU	y_{p2}	0	AU
z_{bi}	0	AU	z_{p1}	0	AU	z_{p2}	0	AU
vx_{bi}	0	$\mathrm{km\,s}^{-1}$	vx_{p1}	0	$\mathrm{km\,s}^{-1}$	vx_{p2}	0	$\mathrm{km\,s}^{-1}$
vy_{bi}	0	$\mathrm{km\,s}^{-1}$	vy_{p1}	23.35	$\mathrm{km\,s}^{-1}$	vy_{p2}	-30.9	$\mathrm{km\,s}^{-1}$
vz_{bi}	0	$\mathrm{km\,s}^{-1}$	vz_{p1}	0	$\mathrm{km\,s}^{-1}$	vz_{p2}	0	$\mathrm{km\,s}^{-1}$

Table 3.2: Initial values for the three sink particles used in the simulations.

the envelope which can be calculated via equation 2.9. Choosing $\alpha_{CE} = 0.75$ and the parameters according to NN Serpentis this leads to $\Delta E_{orb} \simeq 10^{47}$ erg. To account for different values of the efficiency parameter and possible further sources of energy, e.g. nuclear energy, we use $E_{set} = E_{kin}/\Delta E_{orb} = 0.5, 1.0$ and 2.0 with $\Delta E_{orb} = 8.2 \times 10^{46}$ erg.

The values for the varying parameters are presented in Table 3.3. I run simulations with all possible combinations of these parameters. Furthermore, I carry out one simulation with very low kinetic energy in order to approximate the adiabatic case. Figures 3.2 and 3.3 show the initial distribution of density and velocity for a simulation with initial parameters of $E_{set} = 0.5$, $\alpha = 1$, rad $= 0.5$.

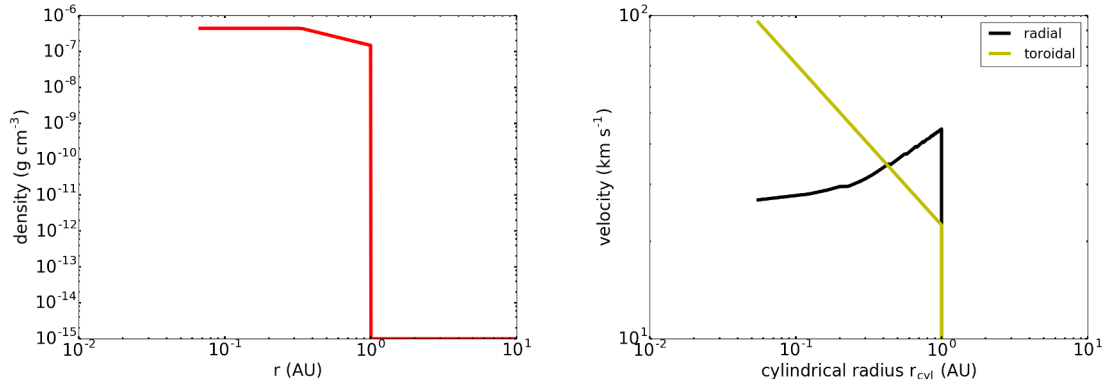| parameter	value 1	value 2	value 3
E_{set}	0.5	1.0	2.0
α	1.0	1.5	2.0
rad	0.5	0.7	1.0

Table 3.3: Variables for the parameter study.

Figure 3.2: Initial distribution of density (left) and velocities (right) for a simulation with $E_{\mathrm{set}} = 0.5, \alpha = 1$, rad = 0.5, zoomed in on the inner part of radius 10 AU. The density is constant within the radius r_{core} and decreases outside r_{core} proportional to $r^{-\alpha}$.
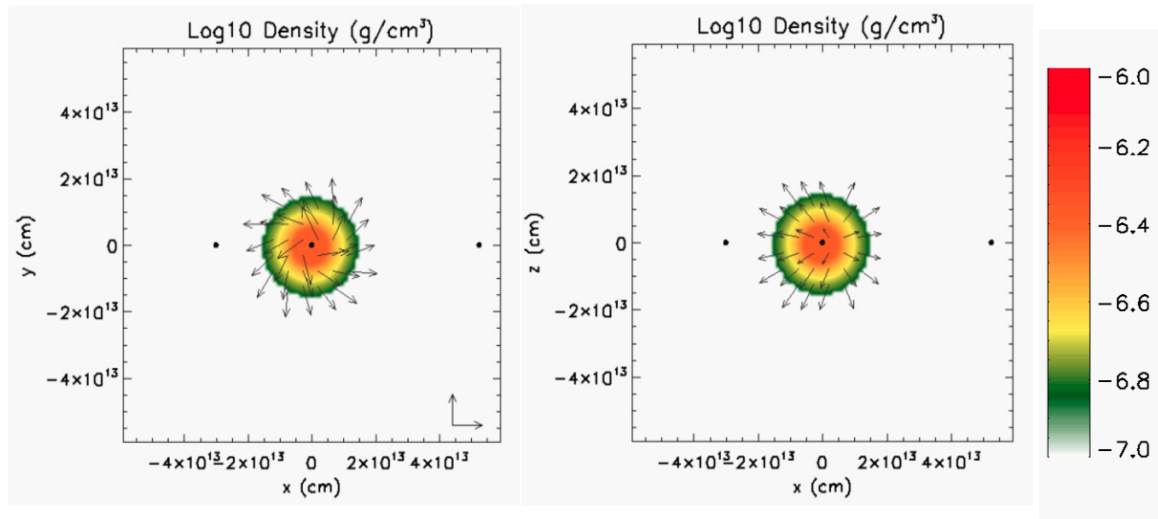

Figure 3.3: Slice in the xy-plane (left) and xz-plane (right) showing initial density and velocity distribution (scaled to $50\,\mathrm{km\,s^{-1}}$) for a simulation with $E_{\mathrm{set}} = 0.5, \alpha = 1$, rad = 0.5. The black dots denote the positons of the binary and the planets.

4
Results

In the following sections, I present the results of the parameter study. All simulations presented here were run at the *Hummel* cluster of the Universität Hamburg.

The cluster consists of 396 compute nodes of which 394 are equipped with 2 CPUs, each containing 8 cores. Out of these, a partition of 54 nodes is additionally equipped with a GPU. The partition of GPU-nodes was used for the performed simulations.

In the first step, the simulations were run for 3072 CPUh or a simulated time of 9.5 years. Simulations showing interesting results in the first step and the prospect of further evolution were restarted. This results in independent runtimes of the simulations ranging between 4 and 15 years.

I will focus on two simulations in detail. These are the simulation with the parameter set $E_{set} = 0.5$, $\alpha = 1$, rad = 0.5 (from now on Simulation 1), and the simulation representing the low-energy case with $E_{kin} \ll E_{int}$ (from now on Simulation 2) in sections 4.1 and 4.2, respectively. Subsequently, I present individual outcomes in sections 4.3 to 4.7.
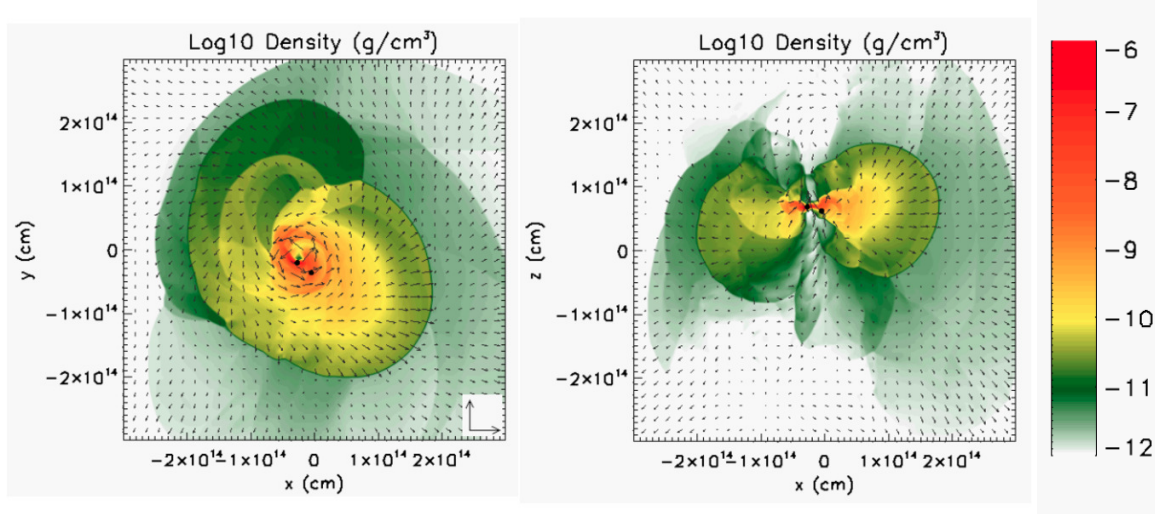
Figure 4.1: Gas density distribution and velocity vectors, scaled to $50 \, \mathrm{km \, s^{-1}}$, of Simulation 1 after 15.5 yrs in xy (left) and xz (right). The slices are chosen close to the maximum density such that $z \sim 4.6$ AU in the left panel and $y \sim -1.3$ AU in the right panel. An asymmetric region of high-density gas has formed, surrounding the binary. The gas rotates in the xy-plane. One planetary sink particle has left the simulation box, two particles are left (black circles).

4.1   Simulation 1 - $\mathrm{E}_{\mathrm{set}} = 0.5$, $\alpha = 1$, rad $= 0.5$

The simulation was run for ~ 15.5 years. The original distribution of gas density and velocity is shown in Fig. 3.2. After 15.5 years the density center is located at the position $x_c = -1.7$ AU, $y_c = -1.3$ AU, $z_c = 4.6$ AU. This is in accordance with the position of the binary. Fig. 4.1 shows the density distribution and velocity vectors at the end of the simulation in slices at $z = z_c$ and $y = y_c$.

At the end of the simulation run a disk has formed around the binary. This can be seen in Fig. 4.2 left side, showing the column density in logarithmic scale in particles per cm^2 in the xy-plane, centered around the density center. The right side of Fig. 4.2 shows an upper limit of the disk mass, also density centered. The calculation takes into account the column density derived over the whole height of the box. The images indicate a disk with radius $2 - 3$ AU and a mass of $\sim 0.5 \mathrm{M}_\odot$ around the density center.

The energy budget is plotted in Fig. 4.3. Kinetic energy is transformed to potential energy during the first 4.5 years. After ~ 8 years the energy components converge to almost constant values. Total energy is not conserved in the simulation because mass that is transported out of the simulation box carries energy away that does no longer contribute to the energy budget.

     The gas mass contained within the simulation box is shown in Fig. 4.4 (left), plotted over
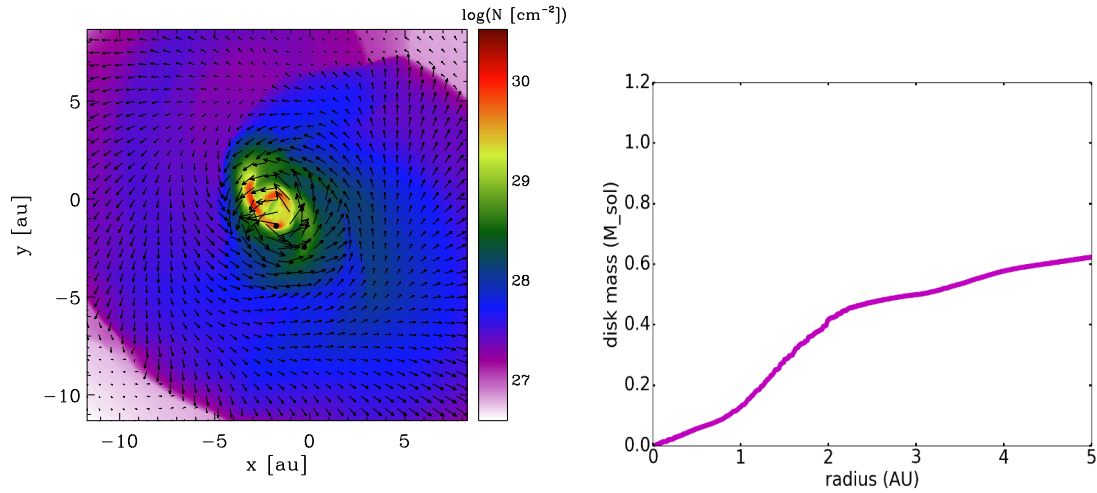
Figure 4.2: Left: column density in the xy-plane for Simulation 1 after 15.5 years. Overplotted are sink particle positions and gas velocity vectors. Right: disk mass plotted versus radius centered at maximum density. The increase of the disk mass declines at a radius of ~ 2 AU. This correspondes well with the drop in column density outside $2-3$ AU of the density center.
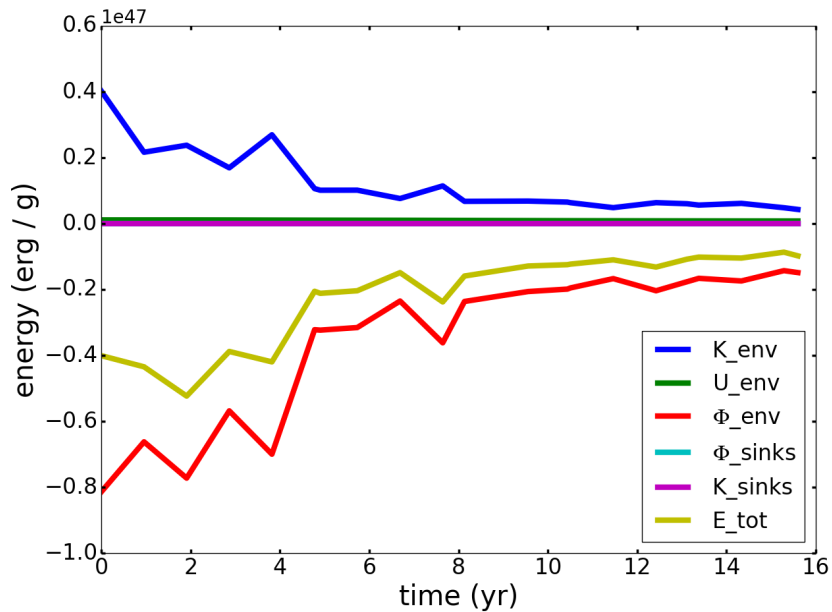

Figure 4.3: Evolution of energy components for Simulation 1. The components e_kin, e_int and e_grav refer to the kinetic, internal and potential energy of the gas. e_sinks denotes the potential energy of the sink particles. The sum of these energy components is plotted as e_tot.
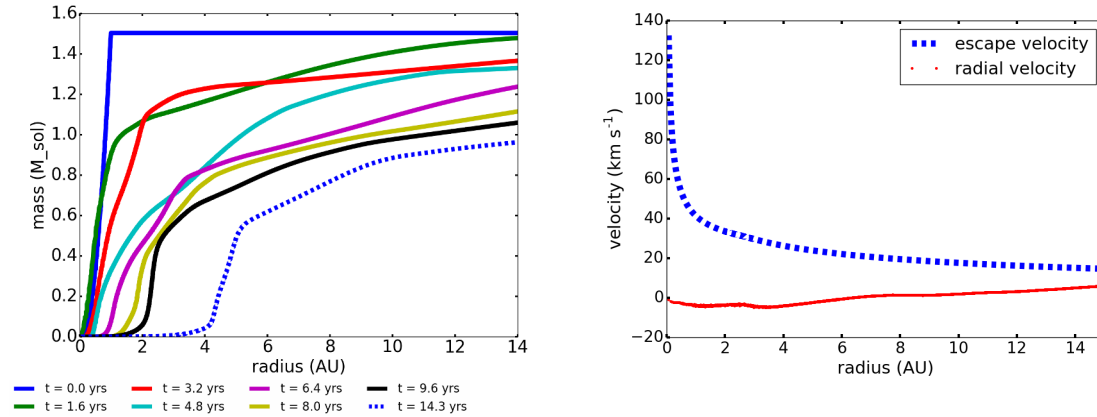
Figure 4.4: Left: Mass enclosed in radius r from the box center for several time steps of Simulation 1. Right: Gas velocity and escape velocity at the end of the simulation plotted over radius r. The enclosed mass at the end of the simulation is bound.

the distance to the center of the simulation box. The fraction of mass contained within the simulation box at the end of the simulation compared to the mass at the beginning of the simulation is roughly 70%. About 50% of the remaining mass is contained within the rotating disk. All the mass within the box at the end of the simulation is gravitationally bound to the system, as can be seen in Fig. 4.4 (right) comparing the radial velocity of the gas and escape velocity.

From the initial two planets only one planet remains bound to the system. The formerly inner planet (planet 2) gets a "kick" after roughly 3 years which accelerates the planet to escape velocity on an outward directed trajectory. The time of the kick corresponds to a time when planet 2 interacts with a high-density region within the envelope (see Fig. 4.5). After ~ 4 years the total velocity of planet 2 clearly exceeds the escape velocity, which can be seen in Fig. 4.6, and we consider the planet as unbound. The planet finally leaves the simulation box after 8 years.
The wake emanating from the outer planet (planet 1), visible in Fig. 4.5, is further discussed in section 4.3. The inflow along the z-axis in the right panel of Fig. 4.5 arises from the initial conditions of the velocity structure within the envelope. Due to the radial motion and rotation around the z-axis, the gas first expands in a double cone structure. The inner region is then filled up with backfalling gas which collides along the z-axis and forms a region with increased density. With the general expansion of the envelope this region expands along the z-axis. The inner parts, closer to the gravitational center, move inwards whereas the outer parts move outwards along the z-axis.
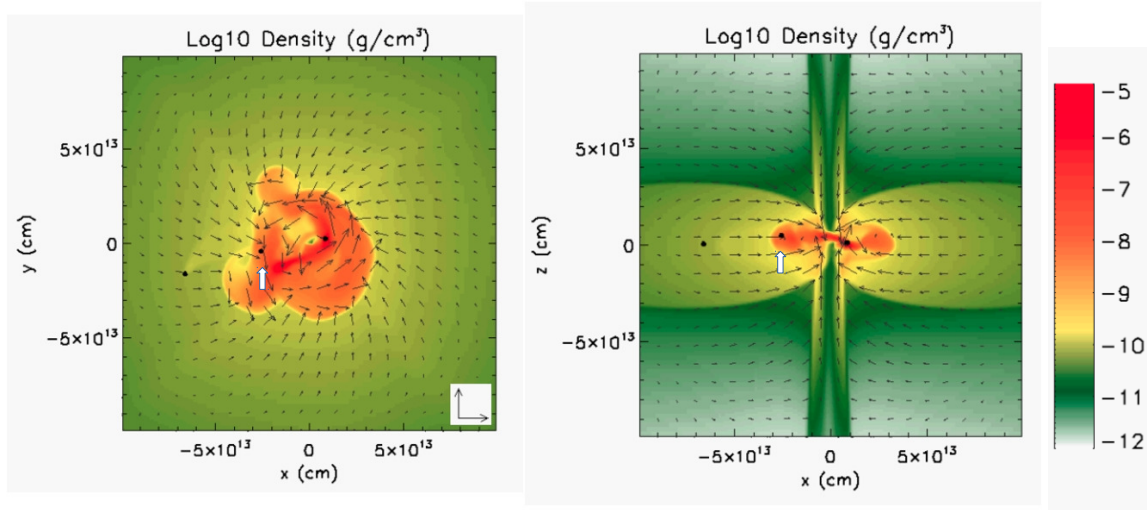
Figure 4.5: Gas density distribution in xy-plane (left) and xz-plane (right) after 2.8 yrs. Velocity vector scaled to $50 \, \mathrm{km \, s^{-1}}$. The gas rotates around the center of mass which lies close to the binary. The inflow along the z-axis arises from the initial conditions. Interaction of the inner planet (marked with arrows) with high-density gas region results in a strong acceleration and leads to the ejection of the planet. The wake at the outer planet is further discussed in section 4.3.
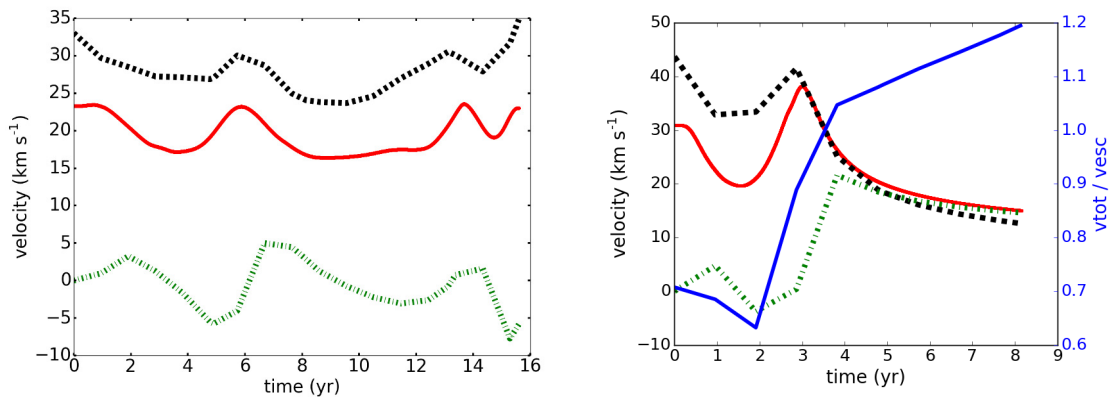

Figure 4.6: Total velocity (red) of planet 1 (left) and 2 (right) compared to the escape velocity (black). The green dashed-dotted line shows the radial velocity of the planet with respect to the center of mass of the system. Blue line in right plot: fraction of total velocity to escape velocity corresponding to blue y-axis on the right side. The outer planet (planet 1) remains bound throughout the simulation while the inner planet is ejected after 4 years and leaves the simulation box after 8 years.
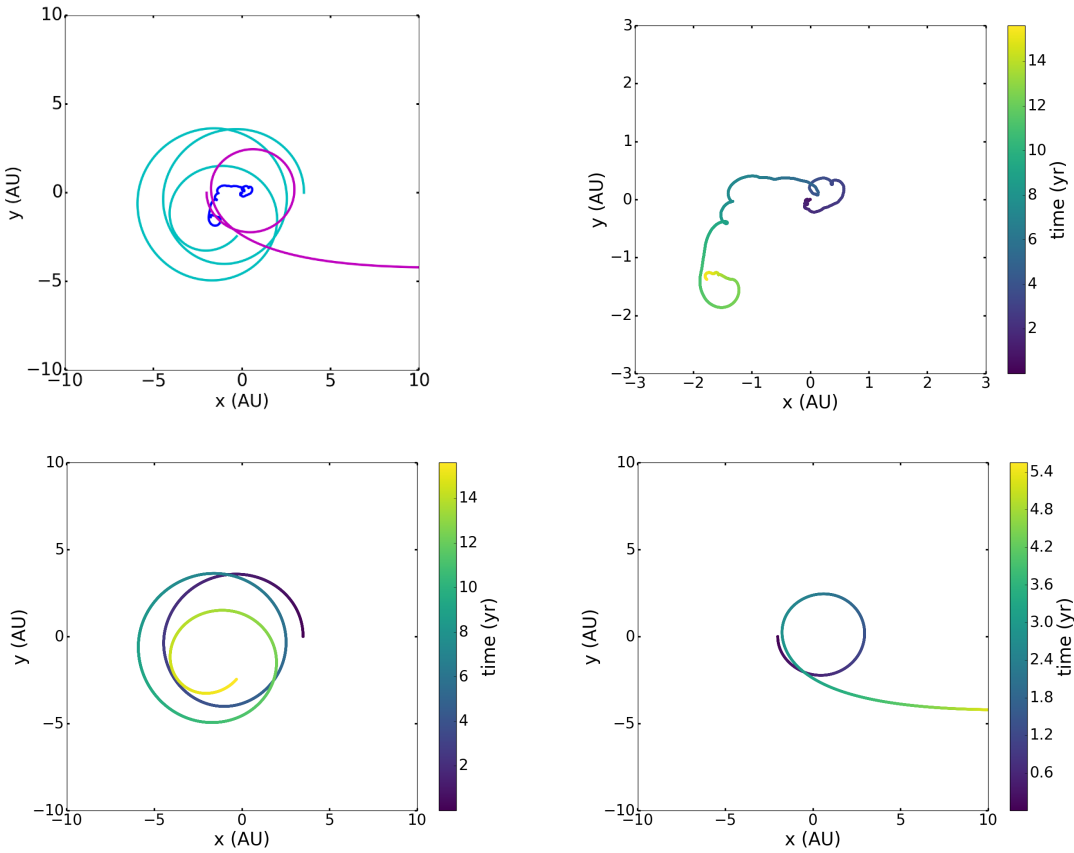
Figure 4.7: Top left: Trajectories of sink particles in the xy-plane, blue: binary, cyan: planet 1, magenta: planet 2. Top right and bottom: Trajectory of the binary (top), planet 1 (bottom left) and planet 2 (bottom right) color coded with time. Note the different axis limits in the top right panel and the differences in the colorbars. The dynamics of planet 1 gets influenced by the gas after 5 years. Planet 2 is accelerated by the gas after 4 years and subsequently is ejected.

Planet 1 remains bound to the system throughout the simulation which can be seen in the velocity of the planet, Fig. 4.6, and the trajectories of the sink particles, Fig. 4.7. After approximately 5 years, the high-density region of the envelope reaches the location of the outer planet as shown in Fig. 4.8. Afterwards, the planetary dynamics is influenced by the gas which leads to the inwards spiral motion of the planet.
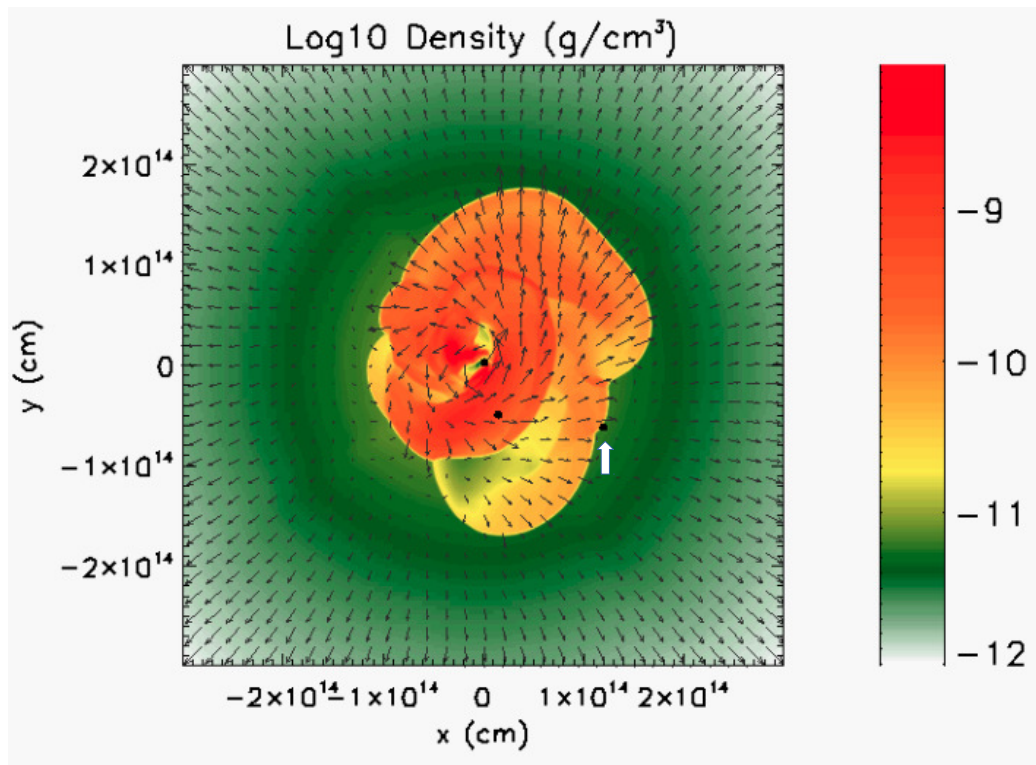
Figure 4.8: Gas density distribution of Simulation 1 in the xy-plane after 5 yrs. The high-density gas region reaches the position of the outer planet which is marked with a white arrow.
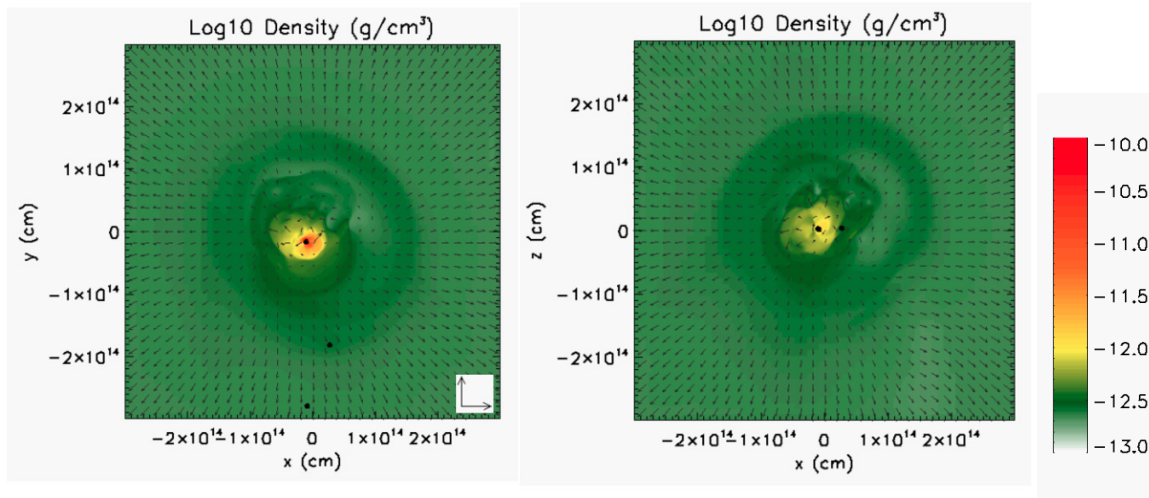
Figure 4.9: Gas density distribution and velocity vectors, scaled to $50\,\mathrm{km\,s^{-1}}$, of Simulation 2 after 10 yrs in xy-plane (left) and xz-plane (right).

4.2   Simulation 2 - low-energy case

The kinetic energy E_{kin} for this simulation was calculated to be of the order of $0.1E_{int}$ with E_{int} being the total internal energy of the envelope. Furthermore, α was set to 1 and rad to 0.5, as is for Simulation 1. Simulation 2 was run for ~ 10 years.

Fig. 4.9 shows the density in xy-plane and xz-plane overplotted with velocity vectors, comparable to Fig. 4.1 for Simulation 1. The gas distribution shows no sign of disk formation, see also the column density structure in Fig. 4.10.

Most of the gas leaves the simulation box within the first 5 years. The fraction of mass remaining within the box at the end is $< 2\%$, shown in Fig. 4.11 (left). The outer parts of this gas reservoir, however, are not gravitationally bound to the system any more, as shows the analysis of the gas velocity Fig. 4.11 (right).

The fast expansion and mass loss lead to a fast reduction of total energy within the simulation box, see Fig. 4.12. This clearly does not represent the adiabatic case. Even with further reduction of the kinetic energy within reasonable limits it was not possible to model the adiabatic expansion of the envelope. Thus, the simulation of the adiabatic case calls for a different simulation setup than is presented here.
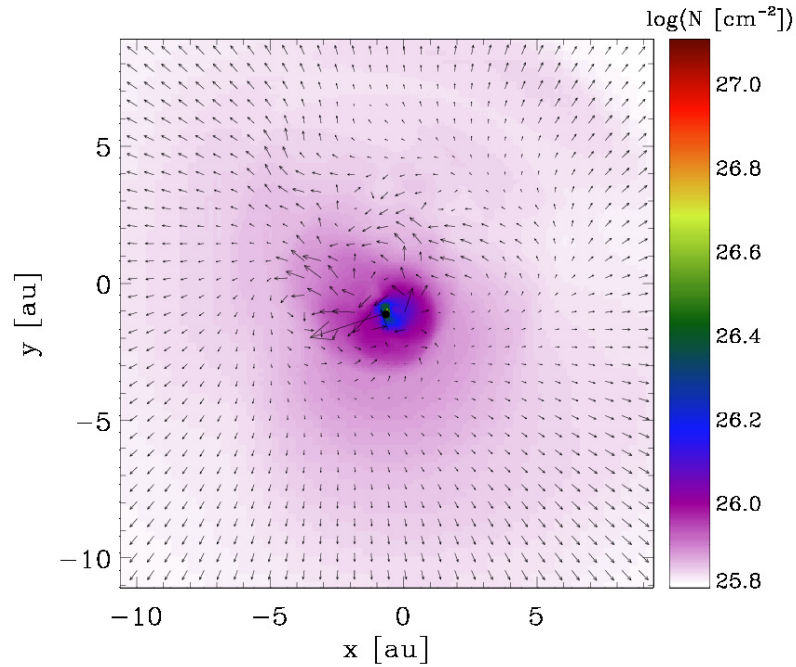
Figure 4.10: Column density in the xy-plane, centered at maximum density, at the end of Simulation 2. The distribution shows no sing of a central disk with high column density and a sharp rim. The gas is not in orbital motion around the center of mass.
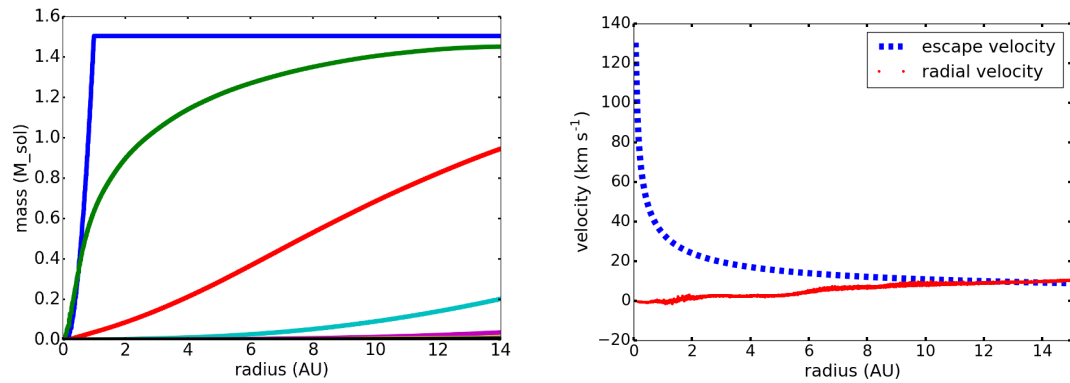

Figure 4.11: Left: Mass enclosed in radius r. The lines are color coded as in Fig. 4.4. After 6.4 years, represented by the magenta line, less than 10% of the initial mass is left inside the simulation box. Right: Gas velocity and escape velocity at the end of the simulation. The gas outside a radius of ~ 13 AU is not gravitationally bound to the system.
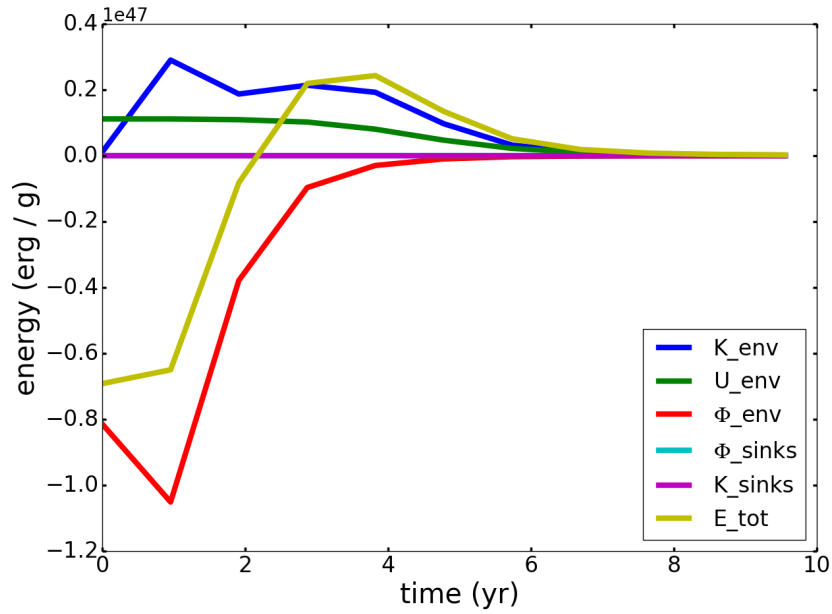
Figure 4.12: Evolution of energy components for Simulation 2. The components are named equivalently to Fig. 4.3. Most of the energy is carried away by gas which leaves the simulation box.

The planets in Simulation 2 move on outwards directed trajectories as would be expected for this rapid mass loss (Fig. 4.13). The analysis of the velocities shows that the inner planet remains gravitationally bound until the end of the simulation run whereas the outer planet exceeds escape velocity after ~ 4 years, see Fig. 4.14.
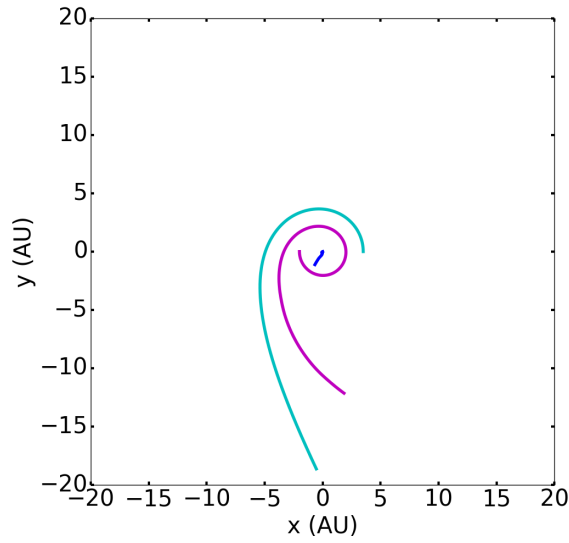
Figure 4.13: Simulation 2: Trajectories of sink particles in the xy-plane. Blue: binary, cyan: outer planet (1), magenta: inner planet (2).
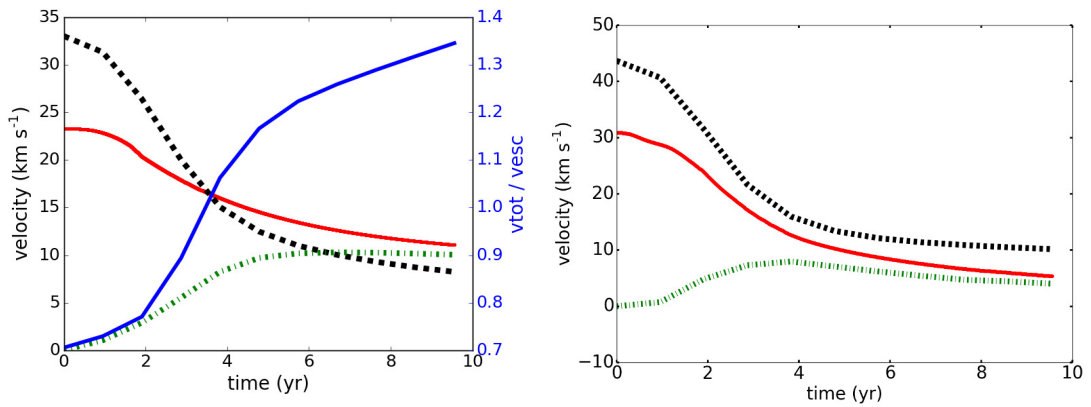

Figure 4.14: Total velocity (red line), escape velocity (black dashed line) and radial velocity with respect to the center of mass (green dashed-dotted line) of planet 1 (left) and 2 (right). The blue line in the left plot shows the ratio of total velocity to escape velocity. After approximately 4 years planet 1 exceeds the escape velocity and is ejected from the system.
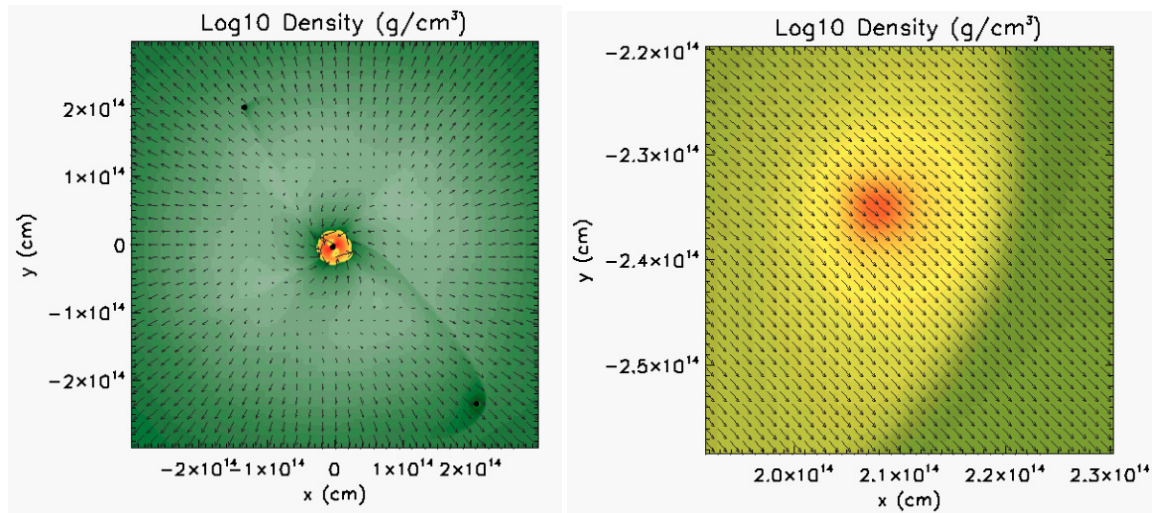
Figure 4.15: Simulation parameters: $E_{set} = 1.0, \alpha = 1.5$, rad = 0.5. Density distribution in the xy-plane overplotted with velocity vectors in xy. Left: full box with sink particles. Right: zoomed in on planetary position. The planet accumulates gas in its surroundings.

4.3 Planet - envelope interaction

In the simulations presented here, the sink particles interact gravitationally with the gas. This means they can accumulate gas, which can be gravitationally bound to the particle. This is obviously the case for the sink particle representing the binary star. In addition, traces of the sink particles representing planets or planetary candidates influencing the gas are also visible within numerous simulations.

One example is shown in Fig. 4.15. The image shows the density distribution in the xy-plane after roughly 5 years overplotted with velocity vectors for the simulation with the following parameters: $E_{set} = 1.0$, $\alpha = 1.5$, rad = 0.5. The density in regions close to the planetary sink particles is clearly higher compared to the surroundings, a wake is formed. This can for example also be seen in Fig. 4.5 in Simulation 1. However, I do not expect the accretion of gas onto the planetary sinks if accretion was enabled. Even in the vicinity of a planetary sink the velocity of the gas is dominated by the expansion and rotation of the envelope. Therefore, the condition of collapse onto the sink particle is not fulfilled.

4.4 Planet trajectories

Some planetary trajectories show remarkable features such as reversals or multiple self-crossings. Examples are given in Fig. 4.16.

The plot on the left side belongs to the simulation with $E_{set} = 0.5$, $\alpha = 1.0$, rad = 0.7. After two orbits, the trajectory of planet 2 turns towards the center of the xy-plane and the binary sink particle, thereby reversing its original direction. The change in the direction is due to interactions with the gas which accelerates the sink particle. A study of this interaction is given in Fig. 4.22 for the simulation with initial parameters $E_{set} = 0.5$, $\alpha = 1.5$, rad = 0.7.

The absolute distance to the binary sink particle, plotted in the bottom panel of Fig. 4.16 decreases to ~ 0.08 AU. However, a re-run of the simulation with sink particle merging activated does not result in the merger of the planet and the binary. This result is physically feasible. Orbital separations of less than 0.1 AU are common for planets, the Exoplanet Data Explorer lists 339 planets in binaries with separations less than 0.1 AU by June 2017.

When the planet approaches the binary sink particle its dynamics is dominated by the gravitational force exerted by the binary resulting in high accelerations. However, both planets remain bound to the system until the end of the simulation as the total velocity is smaller than the escape velocity. This can be seen in the left panels of Fig 4.17 for planet 1 (top) and planet 2 (bottom).

The trajectories plotted on the right side of Fig. 4.16 show the results for the simulation with the following parameters: $E_{set} = 0.5$, $\alpha = 1.5$, rad = 0.5. As a result of the interaction with a high density region of the gas after completing two orbits, the inner planet (planet 2) reverses. The trajectory performs loops, due to the close encounter with the binary, and finally traces the dynamics of the high density region. The velocity of planet 2 oscillates around the escape velocity, see Fig. 4.17 right bottom panel, therefore a prediction whether the planet remains bound or not can not be made without further computations. Planet 1 clearly remains bound to the system.
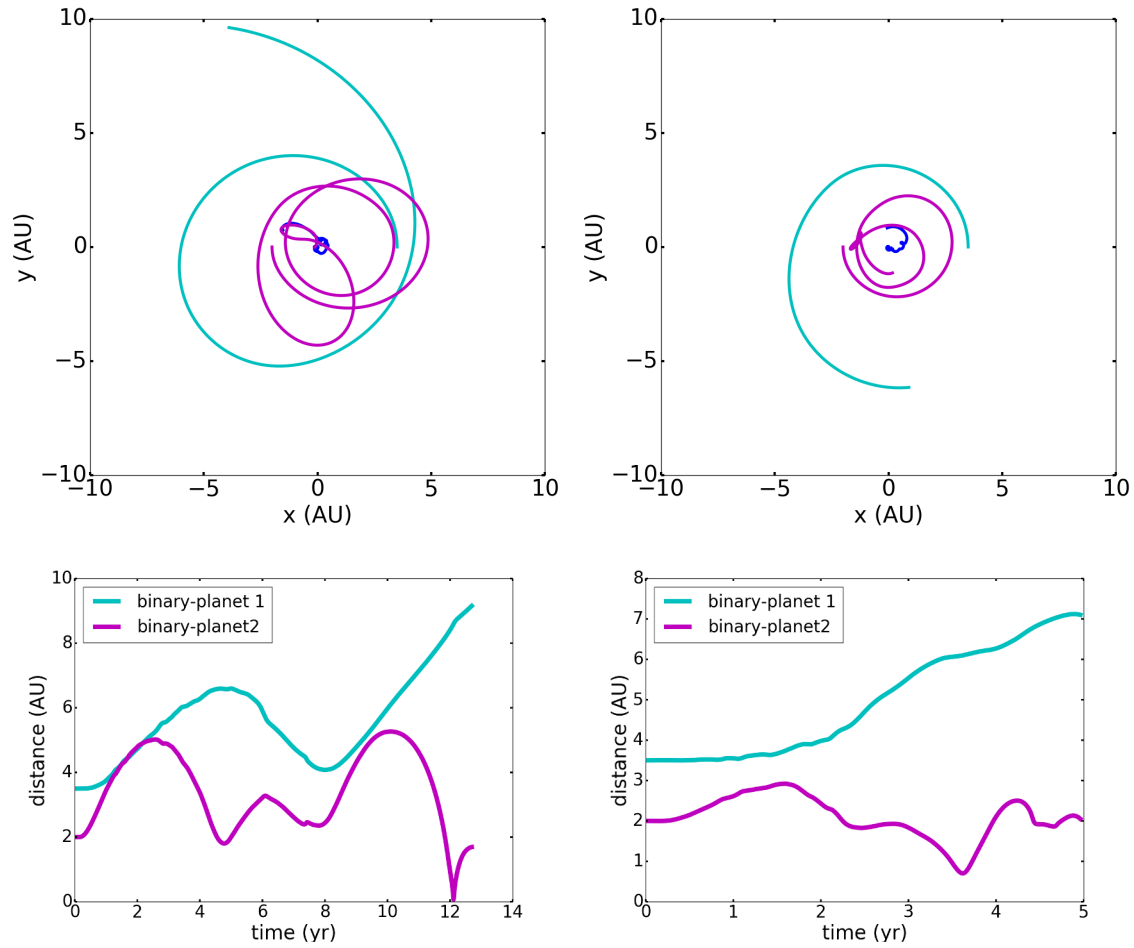
Figure 4.16: Simulation parameters left: $\mathrm{E_{set}} = 0.5, \alpha = 1.0$, rad = 0.7, right: $\mathrm{E_{set}} = 0.5, \alpha = 1.5$, rad = 0.5. Top: trajectories of sink particles in the xy-plane. Bottom: Absolut distance of planet 1 and 2 to the binary sink particle. The loops arise from interactions with high-density gas regions and subsequent close encounters with the binary. Sink particle mergers are excluded due to the high velocities of the planets.
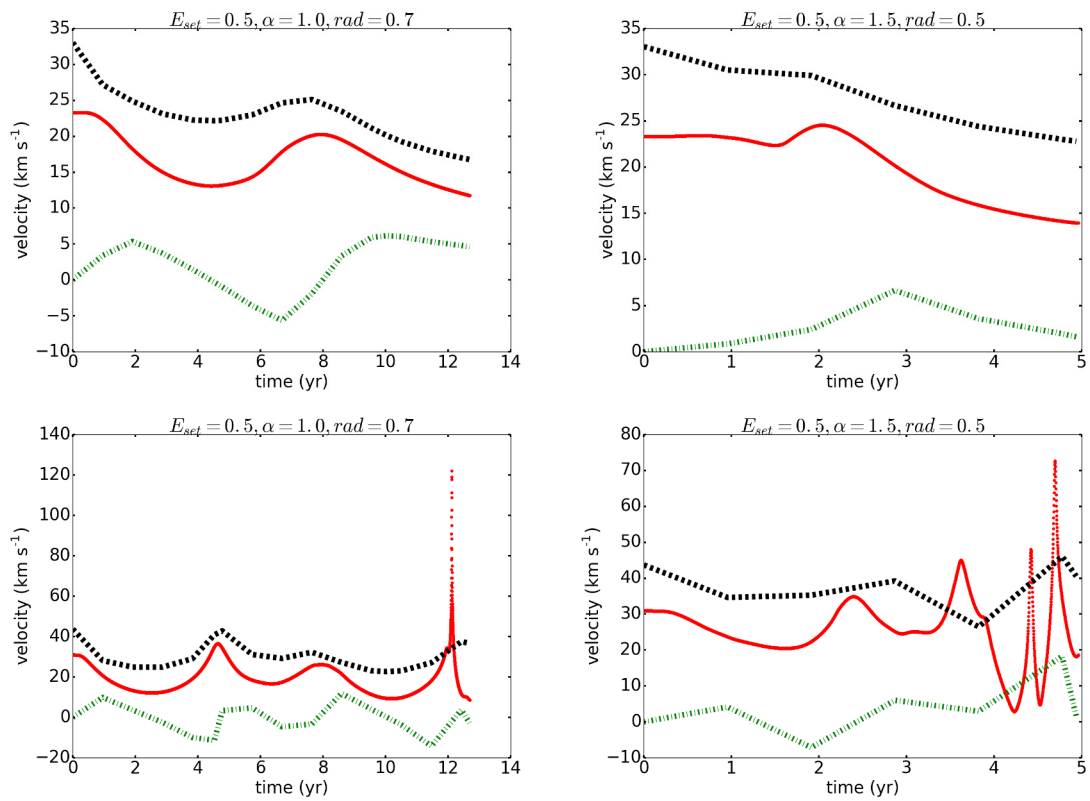
Figure 4.17: Simulation parameters left: $\mathrm{E}_{\mathrm{set}} = 0.5, \alpha = 1.0$, rad = 0.7, right: $\mathrm{E}_{\mathrm{set}} = 0.5, \alpha = 1.5$, rad = 0.5. Plotted are the total (red) and radial (green) velocities of planet 1 (2) in the top (bottom) panel compared to the corresponding escape velocity (black).

4.5 Bound planets

Many planets remain gravitationally bound to the system at the end of the simulation run. These are, in addition to the bound planets presented in sections 4.1, 4.2 and 4.4, the following planets:

1. $E_{set} = 0.5, \alpha = 1.0$, rad = 1.0, planet 1

2. $E_{set} = 0.5, \alpha = 1.5$, rad = 0.7, planets 1 and 2

3. $E_{set} = 0.5, \alpha = 1.5$, rad = 1.0, planets 1 and 2

4. $E_{set} = 0.5, \alpha = 2.0$, rad = 0.5, planets 1 and 2

5. $E_{set} = 0.5, \alpha = 2.0$, rad = 0.7, planets 1 and 2

6. $E_{set} = 0.5, \alpha = 2.0$, rad = 1.0, planets 1 and 2

The velocities of these planets are shown in Fig. 4.18 and 4.19. For comparison, I also show the velocities of the planets for two simulations with $E_{set} = 1.0$ and 2.0, respectively. These are given in Fig. 4.20.
Notice that only for simulations with $E_{set} = 0.5$ and the low-energy case planets remain gravitationally bound. The simulations with one remaining planet have initial density distributions following r^{-1}. This is coherent with the fact that in this case more gas mass is initiated in the outer regions of the envelope and thus has higher radial velocity which leads to fast expansion. The results show no dependence on the parameter rad for the number of planets that remain gravitationally bound.

All planets that remain bound interact with high density regions of the gas. This is exemplified in Fig. 4.22 for the simulation with $E_{set} = 0.5, \alpha = 1.5$, rad = 0.7. The image shows the sink particles with velocity vectors as well as the gas density distribution and velocities in the xy-plane. The first panel (top left) shows the simulation at ~ 1 year. At this time, the initially inner planet (planet 2) is at the right side of the binary sink particle. The velocity vector is directed outwards
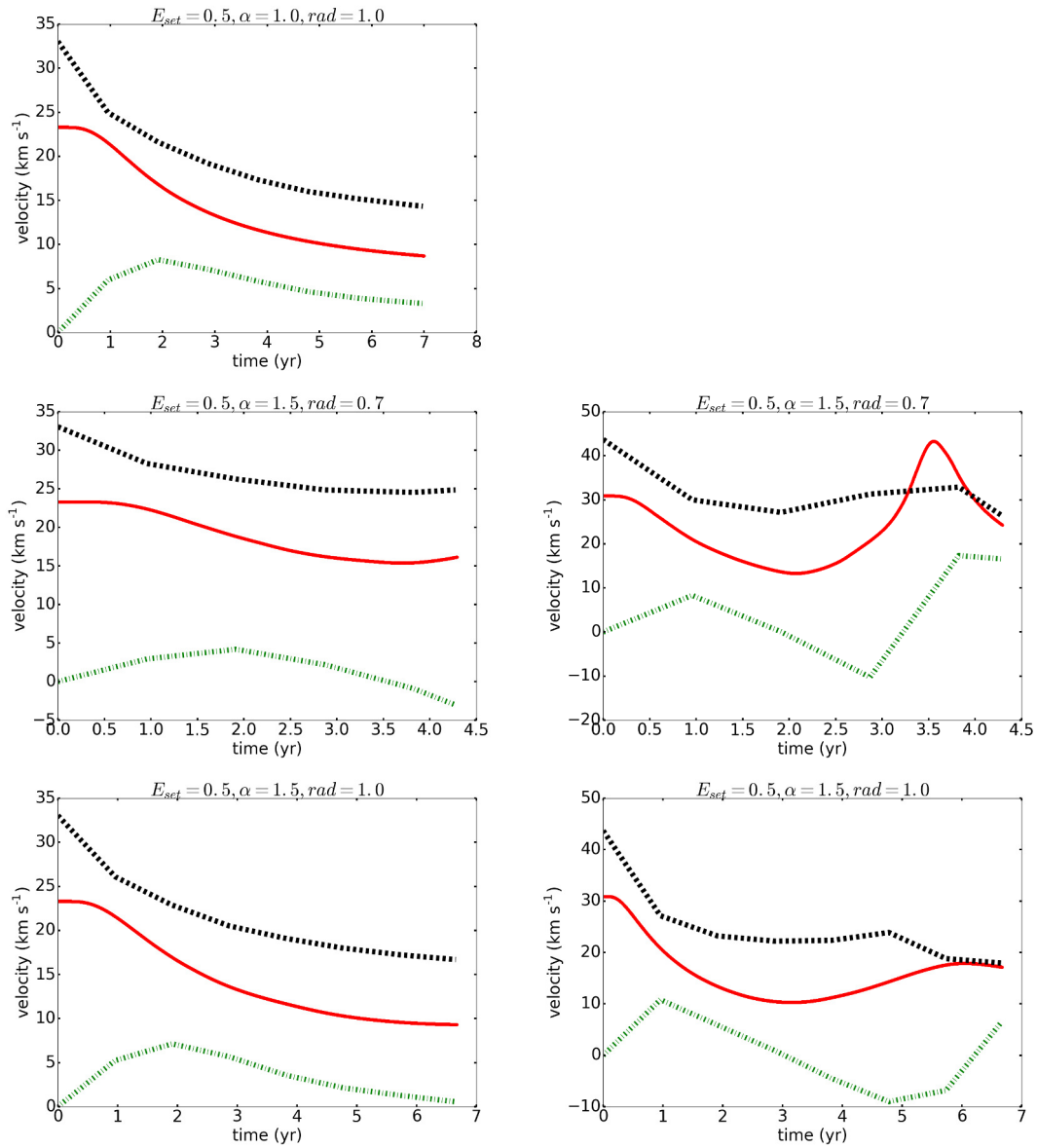
Figure 4.18: Velocities of planets which remain gravitationally bound for the first three simulations of the list in section 4.5. Red line: total velocity, green dashed-dotted line: radial velocity with respect to the center of mass, black dashed line: escape velocity.
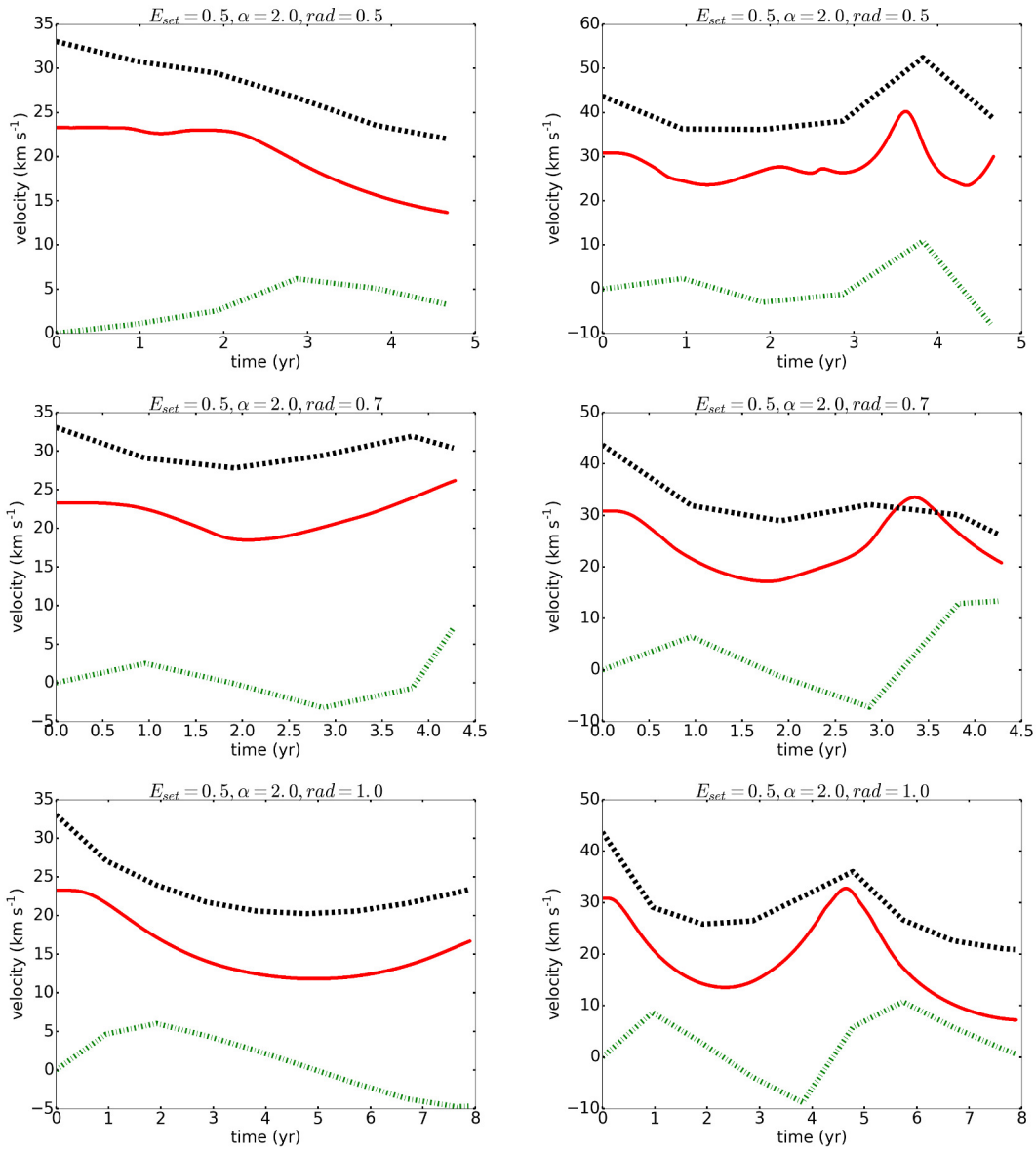
Figure 4.19: As Fig. 4.18 for the last three simulations of the list in section 4.5.
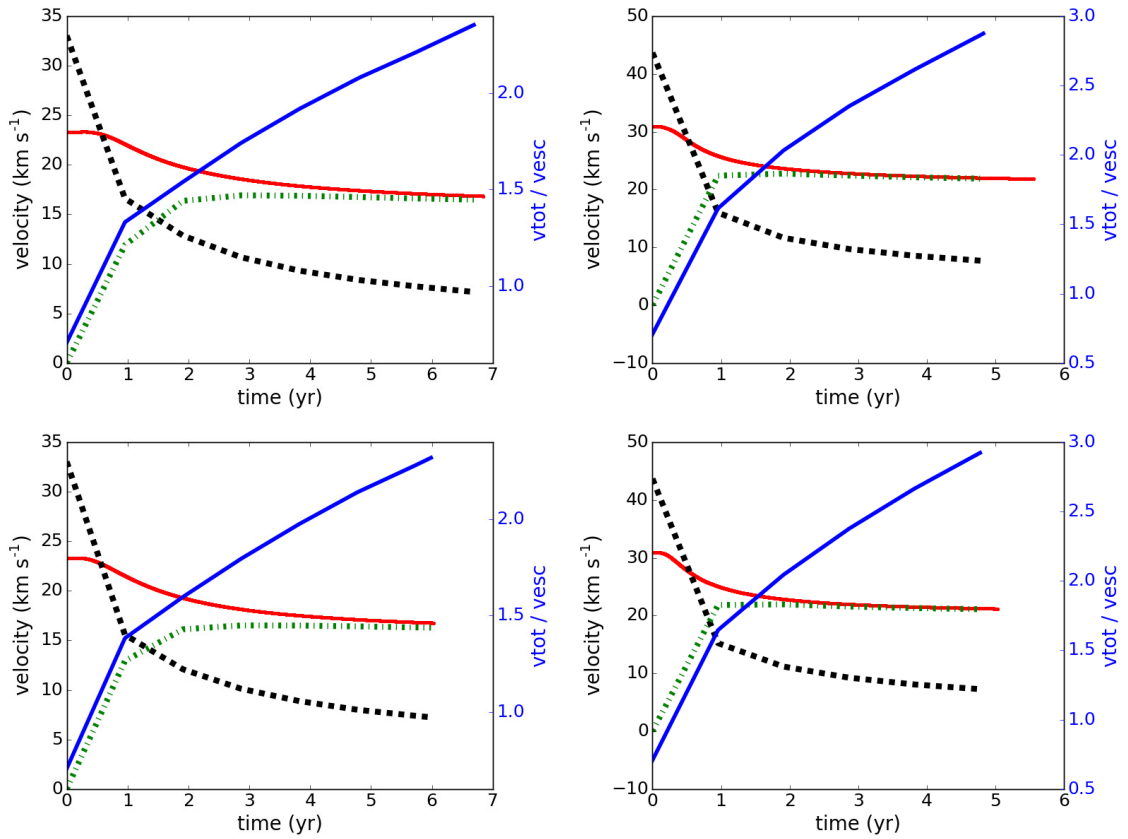
Figure 4.20: Velocities of planets which exceed v_{esc} and are ejected. Top: $E_{set} = 1.0, \alpha = 1.0$, rad = 0.5, bottom: $E_{set} = 2.0, \alpha = 1.0$, rad = 0.5. Left: planet 1, right: planet 2. Total velocity in red, radial velocity in green, escape velocity in black and ratio of total velocity over escape velocity in blue.
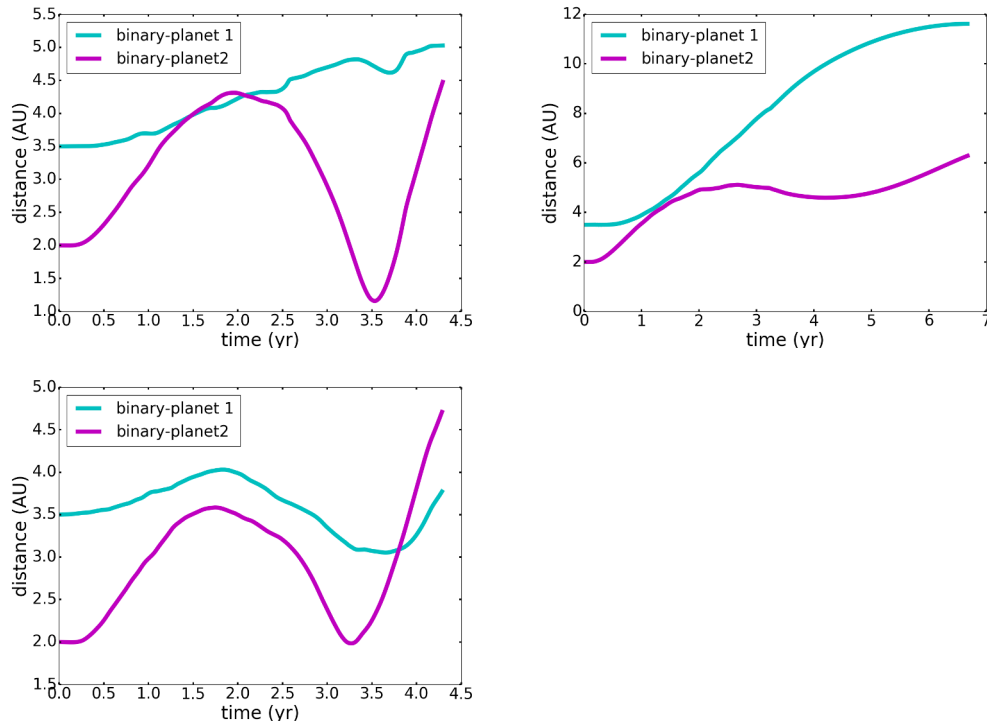
Figure 4.21: Distances of the planets to the binary plotted over time for the simulations with $E_{set} = 0.5, \alpha = 1.5$, rad = 0.7 (top left), $E_{set} = 0.5, \alpha = 1.5$, rad = 1.0 (top right) and $E_{set} = 0.5, \alpha = 2.0$, rad = 0.7 (bottom). For these simulations, the velocity of planet 2 reaches or exceeds the escape velocity (see Fig. 4.18 and 4.19.

compared to the velocity on a circular orbit. In the following, the planet is captured by a high density region and accelerated according to the gas dynamics. The distances of the planets to the binary for the simulations $E_{set} = 0.5, \alpha = 1.5$, rad = 0.7, $E_{set} = 0.5, \alpha = 1.5$, rad = 1.0 and $E_{set} = 0.5, \alpha = 2.0$, rad = 0.7, for which the total velocity of planet 2 reaches or exceeds the escape velocity, are shown in Fig. 4.21. The distances never decrease to less than 1 AU.

The trajectories of planets which have close encounters with the binary are first dominated by the gas dynamics as explained before. Thereby, the planets are forced on trajectories leading towards the binary. Subsequently, the planets are dominated by the binary's gravity which results in very high accelerations as can be seen in Fig. 4.17 in section 4.4. Comparing the distances of these planets to the binary (Fig. 4.16) with the distances plotted in Fig. 4.21 the limit for a close encounter at which the planets dynamics is dominated by the binaries gravity can be set to ~ 1 AU.

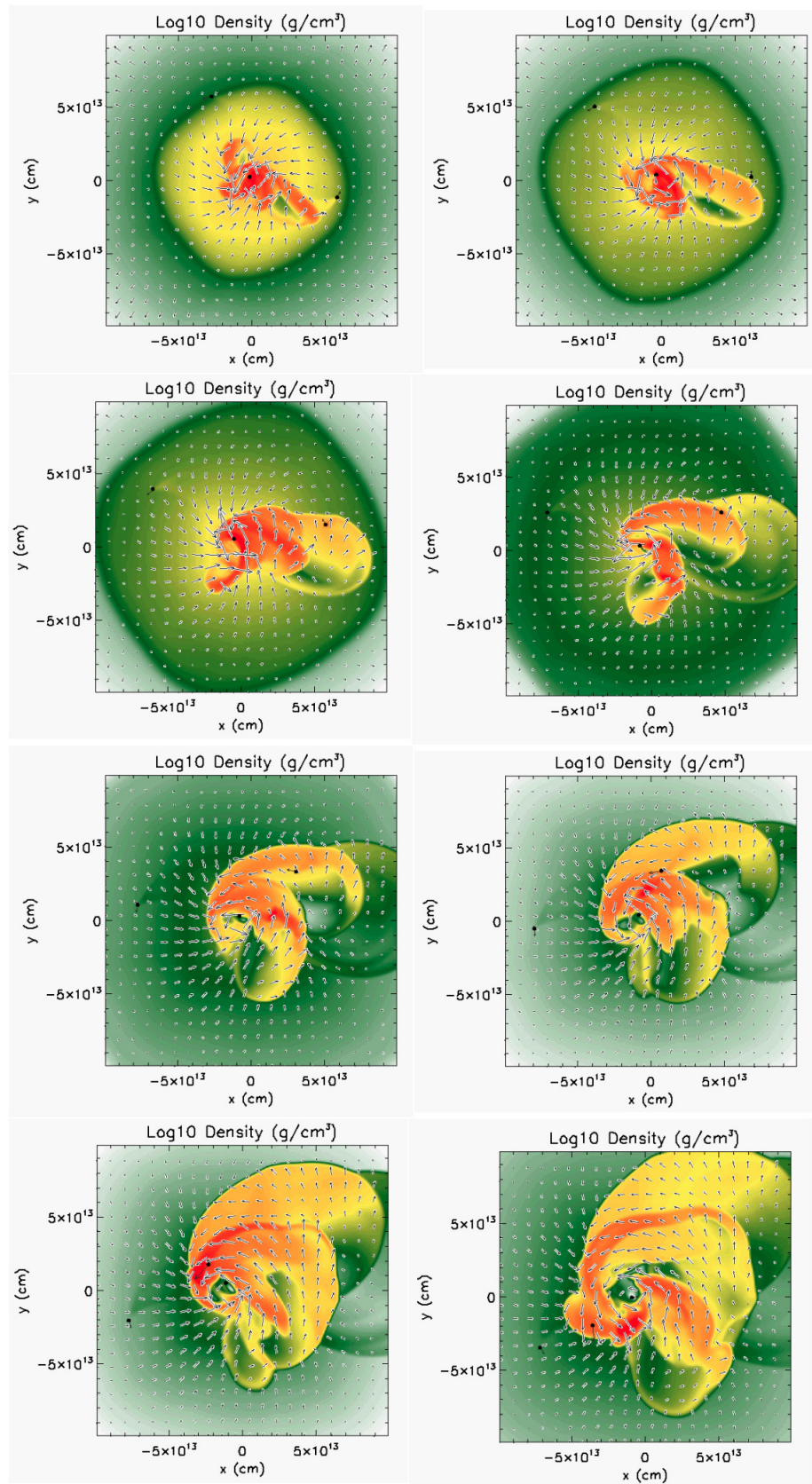**Figure 4.22:** Plots in the xy-plane for simulation with $E_{set} = 0.5, \alpha = 1.5$, rad = 0.7 starting in the top left panel at $t \sim 1$ year, ending in bottom right panel at $t \sim 4$ years. The velocity vectors of the gas, highlited by white borders have the same scaling as the velocity vectors of the sink particles which are plotted in black, attached to the particles (black points).

4.6 Disk formation

The initial conditions are rated as disk forming if the gas distribution fulfills several conditions at the end of the simulation run. These conditions are

1. the column density, computed in the xy-plane, shows a high density region in contrast to the ambient gas

2. the distribution appears visually as disk, i.e. it is flat in z-direction

3. the gas rotates around the density center in the xy-plane

4. the toroidal velocity is much larger than the radial velocity ($v_\phi \gg v_{\mathrm{rad}}$)

In Fig. 4.23 I show column density plots in xy- and xz-plane for one simulation with disk ($E_{\mathrm{set}} = 0.5$, $\alpha = 1.5$, rad = 0.5, left panel) and for one simulation with no disk ($E_{\mathrm{set}} = 0.5$, $\alpha = 1.5$, rad = 1.0, right panel). Compared to the simulation on the left side, the simulation on the right has an extended gas distribution along the z-direction. The gas appears to rotate in the xy-plane, however the fraction of v_ϕ / v_{rad} is rather small.

The simulations which show disks at the end of the simulation runs according to my definition are summarized in table 4.1. Disks are formed for all values of E_{set}, α and rad.
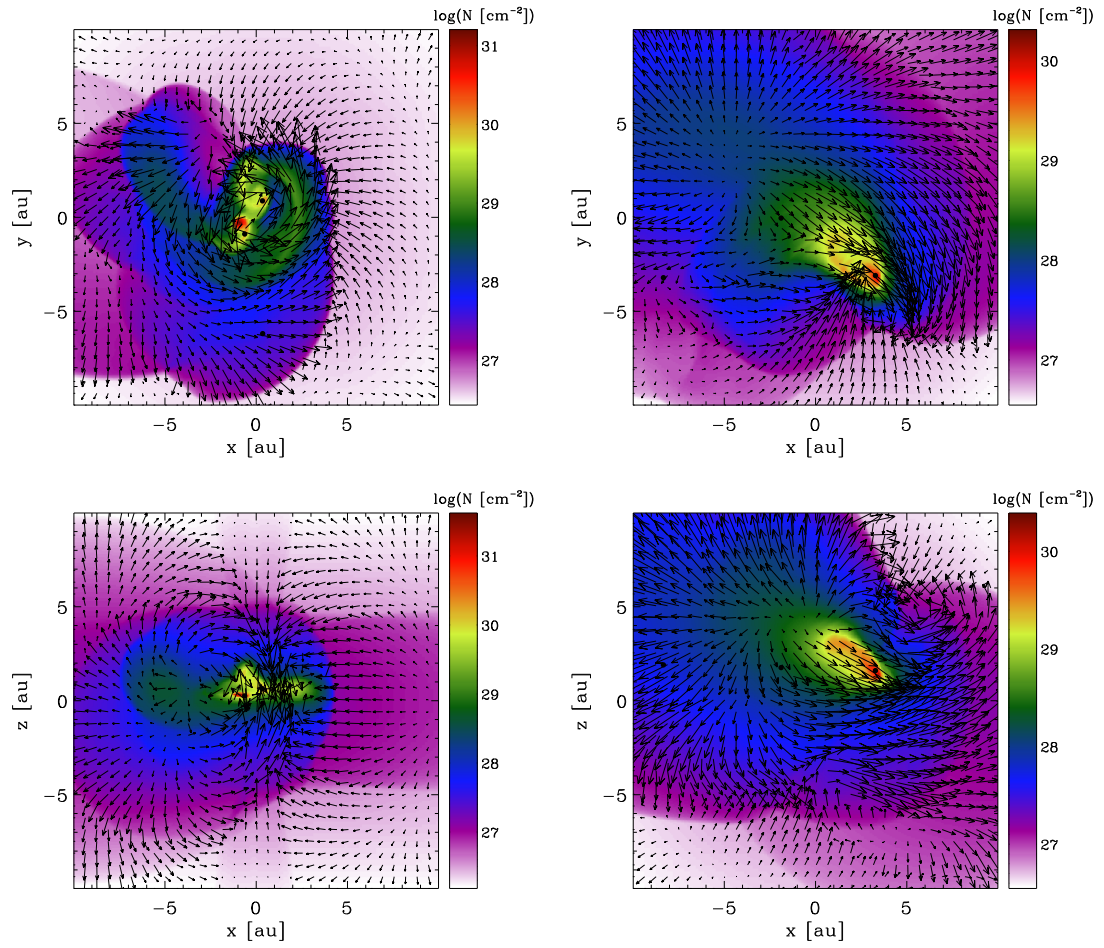
Figure 4.23: Column density plot in xy-plane (top) and xz-plane (bottom), centered on the center of the simulation box, for the simulations $E_{set} = 0.5, \alpha = 1.5$, rad = 0.5 and $E_{set} = 0.5, \alpha = 1.5$, rad = 1.0 in the left, respectively right panel. The black points mark the positions of the binary and the planets. Overplotted are the velocity vectors of the gas. The simulation on the left side is classified as disk-forming. The simulation on the right side does not form a disk.

E_{set}	α	rad	bound planets	remaining mass / initial mass
0.5	1.0	0.5	✓	0.711
0.5	1.0	0.7	✓✓	0.793
1.0	1.0	0.5	✗	0.031
1.0	1.0	0.7	✗	0.097
2.0	1.0	0.5	✗	0.001
2.0	1.0	0.7	✗	0.005
2.0	1.0	1.0	✗	0.05
0.5	1.5	0.5	✓✓	0.944
0.5	1.5	0.7	✓✓	0.908
1.0	1.5	0.5	✗	0.187
1.0	1.5	0.7	✗	0.159
2.0	1.5	0.5	✗	0.003
0.5	2.0	0.5	✓✓	0.956
0.5	2.0	0.7	✓✓	0.918
1.0	2.0	0.5	✗	0.371
1.0	2.0	1.0	✗	0.291
2.0	2.0	0.5	✗	0.004

Table 4.1: Column 1 to 3: initial parameters for simulations which form disks. Column four marks the number of bound planets. The last column gives the gas mass that remains within the simulation box at the end of the simulation run as fraction of the initial mass.

4.7   Remaining mass

Irrespective of the different runtimes do all simulations approximate a stable solution at the end, represented by convergence of the total energy and the remaining (bound) mass. The remaining mass within the simulation box for all simulations, in units of the initial mass, is plotted in Fig. 4.24 against the parameter E_{set}. For better visibility, the values for simulations with $\alpha = 1.0$, plotted in red, are shifted by -0.02 and for $\alpha = 2.0$ (blue) by $+0.02$. The diamonds, squares and circles represent values of rad of 0.5, 0.7 and 1.0, respectively. The green circle represents the low-energy simulation.

As expected, the remaining mass decreases with increasing initial kinetic energy. Furthermore, the remaining mass decreases with increasing α, i.e. for a steeper initial density slope. The dependence on the parameter rad is less strong. Only for the case with $E_{set} = 2.0$ there is a clear trend towards higher values of remaining mass for larger values of rad. The values range from 95% for the simulation with $E_{set} = 0.5$, $\alpha = 2.0$, rad = 0.5 to 0.1% for the initial parameters $E_{set} = 2.0$, $\alpha = 1.0$, rad = 0.5.

The fact that most of the envelope's material remains bound for simulations with $E_{set} < \Delta E_{orb}$ whereas large parts are unbound for simulations with $E_{set} \gtrsim \Delta E_{orb}$ confirms a conclusion by Passy et al. (2012). In their analysis, the authors find that an additional energy input of about $0.1\Delta E_{orb}$ is enough to fully unbind the envelope compared to only unbinding $\sim 15\%$ without additional energy input.
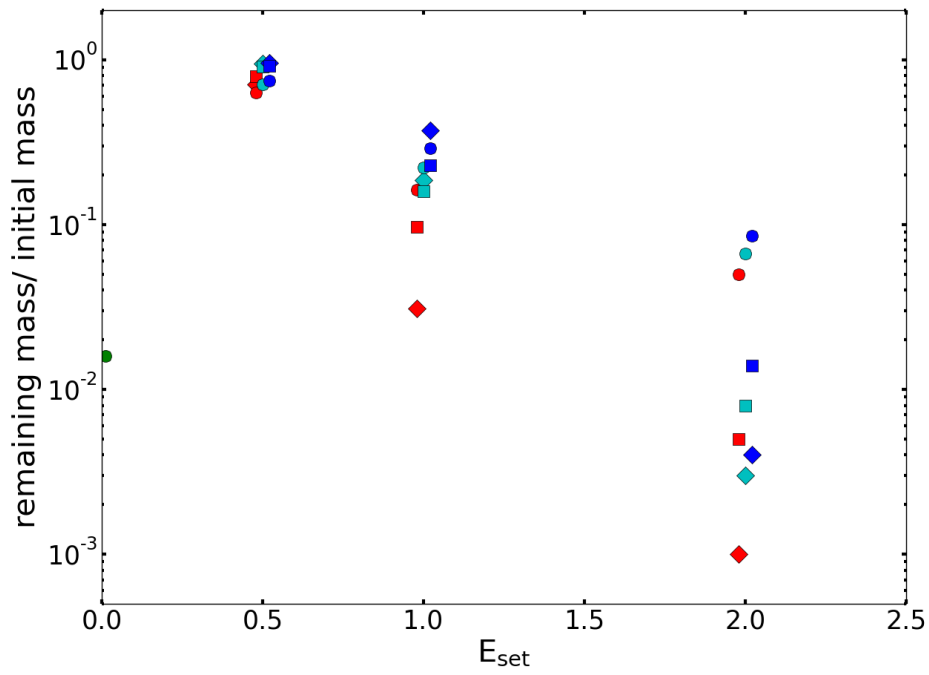
Figure 4.24: Mass within the simulation box at the end of the simulation run in multiples of the initial mass. Simulations with $\alpha = 1.0$ (red) are shifted by -0.02 against E_{set} and simulations with $\alpha = 2.0$ (blue) are shifted by $+0.02$. Cyan signs represent simulations with $\alpha = 1.5$. Values for rad of $0.5, 0.7$ and 1.0 are represented by diamonds, squares and circles, respectively. The low-energy case is represented by a green circle.

<div style="text-align: right">

5

</div>

Conclusion and Outlook

The research on post–common envelope binaries is still in progress. With this thesis I want to contribute to the research by analyzing the interaction of gas and stellar as well as planetary objects during the post–CE phase. The following conclusion summarizes the findings of the performed parameter study presented in chapter 4.

PLANET - GAS INTERACTIONS   On the one hand, the gas is influenced by the planets which can be seen in the formation of wakes behind planets and the formation of highly asymmetric density structures. However, no accretion of gas onto planets is observed in these simulations. On the other hand, the gas influences the planets which may lead to highly deformed trajectories compared to the undisturbed case. This way, planets can remain gravitationally bound to the system or have close encounters with the binary star. The planet - gas interactions depend on the velocity of the gas. The impact is higher for smaller gas velocities, i.e. small values of kinetic energy. In the simulations the kinetic energy is parametrized in terms of the change of orbital energy ΔE_{orb} as calculated for the system NN Serpentis. With $\Delta E_{orb} = 8.2 \times 10^{46}$ ergs I define

the parameter $E_{set} = E_{kin}/\Delta E_{orb}$. Planets that remain bound throughout the simulation are only found in the case of $E_{set} = 0.5$ and for the low-energy case with $E_{kin} \ll E_{int}$ for the envelope.

PLANET - BINARY INTERACTIONS   If a planet is scattered towards the binary by interactions with high density gas regions, its dynamics is dominated by the binary's gravitational potential. Thus, the planet experiences high accelerations. The limiting distance under which the dynamics of the planet is dominated by the binary as determined from the simulations is 1 AU. The trajectories of planets which have close encounters with the binary are irregular and predictions whether the planet remains bound or gets expelled are difficult. Mergers of planets with the binary are not observed and are no physical necessity.

REMAINING MASS AND DISK FORMATION   The fraction of the gas mass which remains bound after a CE event is highly discussed because it is influenced by the energy budget of the CE event. So far, numerical simulations can not reproduce the observations concerning bound gas as well as binary separation. I showed in section 4.7 that the remaining mass highly depends on the amount of energy inserted in the envelope. This is in accordance with the results by Passy et al. (2012). Furthermore, the velocity profile of the envelope can change the amount of remaining gas by up to two orders of magnitude. Over all, the amount of bound gas ranges from 95% to 0.1% of the initial gas mass. This supports the results of Ricker and Taam (2012) who predict that the total mass of the envelope might get ejected as well as the outcomes of the simulation by Ohlmann et al. (2016a) where only 8% of the initial gas mass is unbound.

Schleicher and Dreizler (2014) estimate a bound mass of $0.133 M_\odot$ for the system NN Serpentis. This is $\sim 10\%$ of the initial envelope mass. The calculation is based on the injection of 1.8×10^{47} ergs into the envelope. This value is comparable to my results for the case of $E_{set} = 2$ under the assumption of an exclusively radially expanding envelope. Considering an initially rotating envelope the simulations presented here suggest a lower value for the bound mass of the order of 1% of the initial mass.

Fall-back disks are formed through the interaction of gas and the binary. My simulations show that disks occur for all values of E_{set}, α and rad where α describes the slope of the initial density distribution and rad determines the initial ratio of kinetic energy that is used for radial

expansion of the envelope. However, for disks which do not rotate but only expand radially at the beginning the formation of a disk is rather unlikely. Only 2 of 17 simulations which form disks have no initial toroidal velocity.

The formation of a fall-back disk from an intially rotating envelope was studied in Kuruwita et al. (2016). Compared to my simulations the author use the equation of state for an ideal gas with $\gamma = 5/3$ and study the impact of the temperature of the gas. Starting with a total gas mass in the simulation box of $0.49 M_\odot$ and the gas rotating around the z-axis, the final disk mass ranges from $0.28 M_\odot$ to $0.38 M_\odot$, depending on the initial temperature of the gas. This is about $57 - 77\%$ of the initial mass. The total energy of this simulation is comparable to my Simulation 1 presented in section 4.1. I estimate the mass of the formed disk to be about 33% of the initial gas mass. This is lower than the values obtained by Kuruwita et al. (2016). However, the gas has initial radial velocity in my simulations which could be the reason for this discrepancy.

Outlook The presented parameter study opens the field of numerical simulations for the analysis of planetary dynamics and planet - gas interactions in post–CE systems.

Especially with regard to bound planets this study clearly limits the initial setup for the gas. Based on this result it is possible to analyze the fate of planets depending on initial planetary parameters such as mass, orbital separation or multiplicity. Furthermore, the accretion of gas and accumulation of gas onto planets via collision should be investigated in simulations with higher numerical resoultion than is achieved here which could also be done in a study dedicated to bound planets. Here, the numerical resolution had to be limited in order to restrict the data output.

The wide variety of disks that are formed in my simulations can be compared to studies of formation of second-generation planets, for example Schleicher and Dreizler (2014) and Lichtenberg and Schleicher (2015). In the latter one, the evolution of disks with radii ≥ 10 AU is studied. This is much larger than the radii of disks formed in my simulations. However, fragmentation is observed in various cases of initial disk parameters in Lichtenberg and Schleicher (2015) and is not ruled out for smaller disks.

Analyzing in detail the radius, angular momentum, surface density and disk height of the formed disks can help to improve the estimated probability for second-generation planet formation in systems like NN Serpentis. This remains a task for future work.

Acknowledgments

Bibliography

Applegate, J. H. (1992). A mechanism for orbital period modulation in close binaries. *ApJ*, 385:621–629.

Berger, M. J. and Colella, P. (1989). Local adaptive mesh refinement for shock hydrodynamics. *Journal of Computational Physics*, 82:64–84.

Beuermann, K., Dreizler, S., and Hessman, F. V. (2013). The quest for companions to post-common envelope binaries. IV. The 2:1 mean-motion resonance of the planets orbiting NN Serpentis. *A&A*, 555:A133.

Beuermann, K., Hessman, F. V., Dreizler, S., Marsh, T. R., Parsons, S. G., Winget, D. E., Miller, G. F., Schreiber, M. R., Kley, W., Dhillon, V. S., Littlefair, S. P., Copperwheat, C. M., and Hermes, J. J. (2010). Two planets orbiting the recently formed post-common envelope binary NN Serpentis. *Astronomy and Astrophysics*, 521:L60.

Boley, A. C., Hayfield, T., Mayer, L., and Durisen, R. H. (2010). Clumps in the outer disk by disk instability: Why they are initially gas giants and the legacy of disruption. *Icarus*, 207:509–516.

Borucki, W., Koch, D., Basri, G., Batalha, N., Brown, T., Caldwell, D., Christensen-Dalsgaard, J., Cochran, W., Dunham, E., Gautier, T. N., Geary, J., Gilliland, R., Jenkins, J., Kondo, Y., Latham, D., Lissauer, J. J., and Monet, D. (2008). Finding Earth-size planets in the habitable zone: the Kepler Mission. In Sun, Y.-S., Ferraz-Mello, S., and Zhou, J.-L., editors, *Exoplanets: Detection, Formation and Dynamics*, volume 249 of *IAU Symposium*, pages 17–24.

Brinkworth, C. S., Marsh, T. R., Dhillon, V. S., and Knigge, C. (2006). Detection of a period decrease in NN Ser with ULTRACAM: evidence for strong magnetic braking or an unseen companion. *MNRAS*, 365:287–295.

Camacho, J., Torres, S., García-Berro, E., Zorotovic, M., Schreiber, M. R., Rebassa-Mansergas, A., Nebot Gómez-Morán, A., and Gänsicke, B. T. (2014). Monte Carlo simulations of post-common-envelope white dwarf + main sequence binaries: comparison with the SDSS DR7 observed sample. *A&A*, 566:A86.

Carroll, B. W. and Ostlie, D. A. (2006). *An introduction to modern astrophysics and cosmology*.

Chandrasekhar, S. (1931). The Maximum Mass of Ideal White Dwarfs. *ApJ*, 74:81.

de Kool, M. (1990). Common envelope evolution and double cores of planetary nebulae. *ApJ*, 358:189–195.

Dewi, J. D. M. and Tauris, T. M. (2000). On the energy equation and efficiency parameter of the common envelope evolution. *A&A*, 360:1043–1051.

Doyle, L. R., Carter, J. A., Fabrycky, D. C., Slawson, R. W., Howell, S. B., Winn, J. N., Orosz, J. A., Pŕsa, A., Welsh, W. F., Quinn, S. N., Latham, D., Torres, G., Buchhave, L. A., Marcy, G. W., Fortney, J. J., Shporer, A., Ford, E. B., Lissauer, J. J., Ragozzine, D., Rucker, M., Batalha, N., Jenkins, J. M., Borucki, W. J., Koch, D., Middour, C. K., Hall, J. R., McCauliff, S., Fanelli, M. N., Quintana, E. V., Holman, M. J., Caldwell, D. A., Still, M., Stefanik, R. P., Brown, W. R., Esquerdo, G. A., Tang, S., Furesz, G., Geary, J. C., Berlind, P., Calkins, M. L., Short, D. R., Steffen, J. H., Sasselov, D., Dunham, E. W., Cochran, W. D., Boss, A., Haas, M. R., Buzasi, D., and Fischer, D. (2011). Kepler-16: A Transiting Circumbinary Planet. *Science*, 333:1602.

Dubey, A., Fisher, R., Graziani, C., Jordan, IV, G. C., Lamb, D. Q., Reid, L. B., Rich, P., Sheeler, D., Townsley, D., and Weide, K. (2008). Challenges of Extreme Computing using the FLASH code. In Pogorelov, N. V., Audit, E., and Zank, G. P., editors, *Numerical Modeling of Space Plasma Flows*, volume 385 of *Astronomical Society of the Pacific Conference Series*, page 145.

Eggleton, P. P. (1983). Approximations to the radii of Roche lobes. *ApJ*, 268:368.

Einstein, A. (1936). Lens-Like Action of a Star by the Deviation of Light in the Gravitational Field. *Science*, 84:506–507.

Elliott, P., Bayo, A., Melo, C. H. F., Torres, C. A. O., Sterzik, M., and Quast, G. R. (2014). Search for associations containing young stars (SACY). V. Is multiplicity universal? Tight multiple systems. *A&A*, 568:A26.

Federrath, C., Banerjee, R., Clark, P. C., and Klessen, R. S. (2010). Modeling Collapse and Accretion in Turbulent Gas Clouds: Implementation and Comparison of Sink Particles in AMR and SPH. *ApJ*, 713:269–290.

Fryer, C. L., Rockefeller, G., and Warren, M. S. (2006). SNSPH: A Parallel Three-dimensional Smoothed Particle Radiation Hydrodynamics Code. *ApJ*, 643:292–305.

Fryxell, B., Olson, K., Ricker, P., Timmes, F. X., Zingale, M., Lamb, D. Q., MacNeice, P., Rosner, R., Truran, J. W., and Tufo, H. (2000). FLASH: An Adaptive Mesh Hydrodynamics Code for Modeling Astrophysical Thermonuclear Flashes. *ApJS*, 131:273–334.

Haefner, R., Fiedler, A., Butler, K., and Barwig, H. (2004). Refined system parameters for the pre-cataclysmic binary NN Serpentis. *Astronomy and Astrophysics*, 428:181–190.

Han, E., Wang, S. X., Wright, J. T., Feng, Y. K., Zhao, M., Fakhouri, O., Brown, J. I., and Hancock, C. (2014). Exoplanet Orbit Database. II. Updates to Exoplanets.org. *PASP*, 126:827–837.

Han, Z., Podsiadlowski, P., and Eggleton, P. P. (1995). The formation of bipolar planetary nebulae and close white dwarf binaries. *MNRAS*, 272:800–820.

Han, Z., Podsiadlowski, P., Maxted, P. F. L., Marsh, T. R., and Ivanova, N. (2002). The origin of subdwarf B stars - I. The formation channels. *MNRAS*, 336:449–466.

Herwig, F. (2005). Evolution of Asymptotic Giant Branch Stars. *ARA&A*, 43:435–479.

Hilditch, R. W. (2001). *An Introduction to Close Binary Stars*.

Hurley, J. R., Tout, C. A., and Pols, O. R. (2002). Evolution of binary stars and the effect of tides on binary populations. *MNRAS*, 329:897–928.

Iaconi, R., Reichardt, T., Staff, J., De Marco, O., Passy, J.-C., Price, D., Wurster, J., and Herwig, F. (2017). The effect of a wider initial separation on common envelope binary interaction simulations. *MNRAS*, 464:4028–4044.

Iben, Jr., I. and Livio, M. (1993). Common envelopes in binary star evolution. *PASP*, 105:1373–1406.

Iben, Jr., I. and Tutukov, A. V. (1984). Supernovae of type I as end products of the evolution of binaries with components of moderate initial mass (M not greater than about 9 solar masses). *ApJS*, 54:335–372.

Ivanova, N., Justham, S., Chen, X., De Marco, O., Fryer, C. L., Gaburov, E., Ge, H., Glebbeek, E., Han, Z., Li, X.-D., Lu, G., Marsh, T., Podsiadlowski, P., Potter, A., Soker, N., Taam, R., Tauris, T. M., van den Heuvel, E. P. J., and Webbink, R. F. (2013). Common envelope evolution: where we stand and how we can move forward. *A&A Rev.*, 21:59.

Janson, M., Lafrenière, D., Jayawardhana, R., Bonavita, M., Girard, J. H., Brandeker, A., and Gizis, J. E. (2013). A Multiplicity Census of Intermediate-mass Stars in Scorpius-Centaurus. *ApJ*, 773:170.

Kalomeni, B., Nelson, L., Rappaport, S., Molnar, M., Quintin, J., and Yakut, K. (2016). Evolution of Cataclysmic Variables and Related Binaries Containing a White Dwarf. *ApJ*, 833:83.

Kashi, A. and Soker, N. (2011). A circumbinary disc in the final stages of common envelope and the core-degenerate scenario for Type Ia supernovae. *Mon.Not.R.Aston.Soc.*, 417:1466–1479.

Kippenhahn, R. and Weigert, A. (1994). *Stellar Structure and Evolution*.

Krumholz, M. R., McKee, C. F., and Klein, R. I. (2004). Embedding Lagrangian Sink Particles in Eulerian Grids. *ApJ*, 611:399–412.

Kuruwita, R. L., Staff, J., and De Marco, O. (2016). Considerations on the role of fall-back discs in the final stages of the common envelope binary interaction. *MNRAS*, 461:486–496.

Lichtenberg, T. and Schleicher, D. R. G. (2015). Modeling gravitational instabilities in self-gravitating protoplanetary disks with adaptive mesh refinement techniques. *A&A*, 579:A32.

Livio, M. and Soker, N. (1988). The common envelope phase in the evolution of binary stars. *ApJ*, 329:764–779.

Lukat, G. and Banerjee, R. (2016). A {GPU} accelerated barnes–hut tree code for {FLASH4}. *New Astronomy*, 45:14 – 28.

MacNeice, P., Olson, K. M., Mobarry, C., de Fainchtein, R., and Packer, C. (2000). PARAMESH: A parallel adaptive mesh refinement community toolkit. *Computer Physics Communications*, 126:330–354.

Mason, B. D., Hartkopf, W. I., Gies, D. R., Henry, T. J., and Helsel, J. W. (2009). The High Angular Resolution Multiplicity of Massive Stars. *AJ*, 137:3358–3377.

Mayor, M. and Queloz, D. (1995). A Jupiter-mass companion to a solar-type star. *Nature*, 378:355–359.

Meyer, F. and Meyer-Hofmeister, E. (1979). Formation of cataclysmic binaries through common envelope evolution. *A&A*, 78:167–176.

Nandez, J. L. A. and Ivanova, N. (2016). Common envelope events with low-mass giants: understanding the energy budget. *MNRAS*, 460:3992–4002.

Nelemans, G., Verbunt, F., Yungelson, L. R., and Portegies Zwart, S. F. (2000). Reconstructing the evolution of double helium white dwarfs: envelope loss without spiral-in. *A&A*, 360:1011–1018.

Ohlmann, S. T., Röpke, F. K., Pakmor, R., and Springel, V. (2016a). Hydrodynamic Moving-mesh Simulations of the Common Envelope Phase in Binary Stellar Systems. *ApJ*, 816:L9.

Ohlmann, S. T., Röpke, F. K., Pakmor, R., Springel, V., and Müller, E. (2016b). Magnetic field amplification during the common envelope phase. *MNRAS*, 462:L121–L125.

Ollivier, M., Roques, F., Casoli, F., Encrenaz, T., and Selsis, F. (2009). *Planetary Systems*.

O'Shea, B. W., Bryan, G., Bordner, J., Norman, M. L., Abel, T., Harkness, R., and Kritsuk, A. (2004). Introducing Enzo, an AMR Cosmology Application. *ArXiv Astrophysics e-prints*.

Paczyński, B. (1971). Evolutionary Processes in Close Binary Systems. *ARA&A*, 9:183.

Paczynski, B. (1976). Common Envelope Binaries. In Eggleton, P., Mitton, S., and Whelan, J., editors, *Structure and Evolution of Close Binary Systems*, volume 73 of *IAU Symposium*, page 75.

Parsons, S. G., Marsh, T. R., Bours, M. C. P., Littlefair, S. P., Copperwheat, C. M., Dhillon, V. S., Breedt, E., Caceres, C., and Schreiber, M. R. (2014). Timing variations in the secondary eclipse of NN Ser. *MNRAS*, 438:L91–L95.

Parsons, S. G., Marsh, T. R., Copperwheat, C. M., Dhillon, V. S., Littlefair, S. P., Gänsicke, B. T., and Hickman, R. (2010). Precise mass and radius values for the white dwarf and low mass M dwarf in the pre-cataclysmic binary NN Serpentis. *MNRAS*, 402:2591–2608.

Passy, J.-C., De Marco, O., Fryer, C. L., Herwig, F., Diehl, S., Oishi, J. S., Mac Low, M.-M., Bryan, G. L., and Rockefeller, G. (2012). Simulating the Common Envelope Phase of a Red Giant Using Smoothed-particle Hydrodynamics and Uniform-grid Codes. *The Astrophysical Journal*, 744:52.

Podsiadlowski, P. (2001). Common-Envelope Evolution and Stellar Mergers. In Podsiadlowski, P., Rappaport, S., King, A. R., D'Antona, F., and Burderi, L., editors, *Evolution of Binary and Multiple Star Systems*, volume 229 of *Astronomical Society of the Pacific Conference Series*, page 239.

Podsiadlowski, P., Ivanova, N., Justham, S., and Rappaport, S. (2010). Explosive common-envelope ejection: implications for gamma-ray bursts and low-mass black-hole binaries. *MN-RAS*, 406:840–847.

Rebassa-Mansergas, A., Gänsicke, B., Rodriguez-Gil, P., Schreiber, M., and Koester, D. (2007). Post-common-envelope binaries from SDSS - I. 101 white dwarf main-sequence binaries with multiple Sloan Digital Sky Survey spectroscopy. *Mon.Not.R.Aston.Soc.*, 382:1377–1393.

Ricker, P. M. and Taam, R. E. (2008). The Interaction of Stellar Objects within a Common Envelope. *The Astrophysical Journal*, 672:L41–L44.

Ricker, P. M. and Taam, R. E. (2012). An AMR Study of the Common-envelope Phase of Binary Evolution. *The Astrophysical Journal*, 746:74.

Rohrmann, R. D., Althaus, L. G., García-Berro, E., Córsico, A. H., and Miller Bertolami, M. M. (2012). Outer boundary conditions for evolving cool white dwarfs. *A&A*, 546:A119.

Schleicher, D. R. G. and Dreizler, S. (2014). Planet formation from the ejecta of common envelopes. *A&A*, 563:A61.

Schleicher, D. R. G., Dreizler, S., Völschow, M., Banerjee, R., and Hessman, F. V. (2015). Planet formation in post-common-envelope binaries. *Astronomische Nachrichten*, 336:458.

Truelove, J. K., Klein, R. I., McKee, C. F., Holliman, II, J. H., Howell, L. H., and Greenough, J. A. (1997). The Jeans Condition: A New Constraint on Spatial Resolution in Simulations of Isothermal Self-gravitational Hydrodynamics. *ApJ*, 489:L179–L183.

van den Heuvel, E. P. J. (1976). Late Stages of Close Binary Systems. In Eggleton, P., Mitton, S., and Whelan, J., editors, *Structure and Evolution of Close Binary Systems*, volume 73 of *IAU Symposium*, page 35.

Veras, D. (2016). Post-main-sequence planetary system evolution. *Royal Society Open Science*, 3:150571.

Völschow, M., Banerjee, R., and Hessman, F. V. (2014). Second generation planet formation in NN Serpentis? *Astronomy and Astrophysics*, 562:A19.

Waagan, K., Federrath, C., and Klingenberg, C. (2011). A robust numerical scheme for highly compressible magnetohydrodynamics: Nonlinear stability, implementation and tests. *Journal of Computational Physics*, 230:3331–3351.

Wang, C., Jia, K., and Li, X.-D. (2016). The binding energy parameter for common envelope evolution. *Research in Astronomy and Astrophysics*, 16:126.

Ward-Duong, K., Patience, J., De Rosa, R. J., Bulger, J., Rajan, A., Goodwin, S. P., Parker, R. J., McCarthy, D. W., and Kulesa, C. (2015). The M-dwarfs in Multiples (MINMS) survey - I. Stellar multiplicity among low-mass stars within 15 pc. *MNRAS*, 449:2618–2637.

Webbink, R. F. (1975). *The evolution of low-mass close binary systems*. PhD thesis, University of Cambridge.

Webbink, R. F. (1984). Double white dwarfs as progenitors of R Coronae Borealis stars and Type I supernovae. *The Astrophysical Journal*, 277:355–360.

Weigert, A., Wendker, H., and Wisotzki, L. (2010). *Astronomie und Astrophysik: Ein Grundkurs*.

Zorotovic, M. and Schreiber, M. R. (2013). Origin of apparent period variations in eclipsing post-common-envelope binaries. *Astronomy and Astrophysics*, 549:A95.

Zorotovic, M., Schreiber, M. R., Gänsicke, B. T., and Nebot Gómez-Morán, A. (2010). Post-common-envelope binaries from SDSS. IX: Constraining the common-envelope efficiency. *A&A*, 520:A86.

Zorotovic, M., Schreiber, M. R., García-Berro, E., Camacho, J., Torres, S., Rebassa-Mansergas, A., and Gänsicke, B. T. (2014). Monte Carlo simulations of post-common-envelope white dwarf + main sequence binaries: The effects of including recombination energy. *A&A*, 568:A68.

Zuo, Z.-Y. and Li, X.-D. (2014). Common Envelope Mechanisms: Constraints from the X-Ray Luminosity Function of High-mass X-Ray Binaries. *ApJ*, 797:45.

Eidesstattliche Versicherung

Hiermit erkläre ich an Eides statt, dass ich die vorliegende Dissertationsschrift selbst verfasst und keine anderen als die angegebenen Quellen und Hilfsmittel benutzt habe.

Die eingereichte schriftliche Fassung entspricht der auf dem elektronischen Speichermedium.

Die Dissertation wurde in der vorgelegten oder einer ähnlichen Form nicht schon einmal in einem früheren Promotionsverfahren angenommen oder als ungenügend beurteilt.

Hamburg, den 20. August 2017

C. Schneide

(Christiane Schneide)